Film Dosimetry of Intensity Modulated Beams

Kahena Chaal

Medical physics Unit

McGill University
Montreal, Quebec, Canada
April 2009

A thesis submitted to the Faculty of Graduate Studies and Research in partial fulfillment of the requirements of the degree of Master of Sciences in Medical Radiation Physics

DEDICATION

This thesis is dedicated to my parents and my husband Abdelmoumene.

ACKNOWLEDGMENTS

This work was conducted in the Departments of Medical Physics and Radiation Oncology of the Montreal General Hospital (MGH) in affiliation with McGill University in Montreal, Canada.

First of all, I am grateful to my supervisor, William Parker, for his guidance and his patience all along this year. William gave me the opportunity and the freedom to work on a practical subject, and he was approachable despite his many responsibilities. I wish also to thank my co-supervisor, Russell Ruo for his precious help in the clinic as well as his remarks that were always pertinent.

I truly do appreciate the kind help of Dr. Gyorgy Hegyi with computed radiography as well as the team of biomedical engineers, particularly,
Jean Rene Benit who made available to me a digitizer just for the aim of this study. I would like also to acknowledge Dr. Wieslaw Wierzbicki from Maisonneuve Rosemont hospital for allowing me to use their CR system as well as Dr. Genevieve Jarry for her precious help.

I am indebted to Dr. Slobodan Devic, who gave me a lot of his precious time. The discussions with him push me always to think further.

Dr. Wamied Abdel-Rahman has never refused his assistance, he was present during the first year of studies and at each time I have asked his help, I really appreciate it. I wish also to thank Michael Evans for providing me with the useful data of the linac.

I would like to acknowledge Professor Podgorsak who contributes to give the best teaching quality in Medical Physics, as well as Margery Knewstubb, the department secretary. I also thank the students involved in this program of medical physics who never refuse to offer their help, particularly, Jason Yan, Yong Chen, Emily Poon and Juergen Last.

And most importantly, I thank my parents who have always encouraged me to go further. Without my husband, it would not be possible to enter the program of Medical Physics, I would like to thank him for his understanding, patience and continuous support.

TABLE OF CONTENTS

LIST OF TABLES

LIST OF FIGURES

ABSTRACT

Intensity modulated beams use complicated computerized treatment planning systems; this makes a manual verification of the number of monitor units difficult to perform. Consequently, before treatment, patient-specific quality assurance must be done in order to ensure that the delivery agrees with the plan; this process involves a measurement of 2D dose distribution in a phantom. In this thesis, first, a photostimulable phosphor luminescence device (also referred to as computed radiography or CR) was evaluated for dosimetric purposes. The proposed protocol showed linearity response of the CR, but energy and field size dependence were discovered. Second, two widely used films for IMRT QA were compared: the radiological film, EDR2, and the radiochromic film, EBT, with the use of the scanner EPSON1680 and the software FILMQA. Results showed that in the relative dose mode, EDR2 gives higher number of pixels passing a chosen criterion compared to EBT. This fact is attributed to the highest contrast observed with EDR2; therefore, any change on pixel value due to scanner artifacts will have less impact on dose calculations with EDR2. Finally, the impact of scanner artifacts on dose assessment with EBT films, processed with FILMQA and a program written on MATLAB, was studied. A correction was introduced on MATLAB that proves the importance of taking scanner artifacts into account for the measurements with the scanner EPSON1680 and EBT films digitized in the portrait orientation. Comparison between FILMQA and MATLAB was performed on profile’s measurements and on fifteen head and neck IMRT QA cases. This comparison showed that one case out of fifteen was drastically improved with MATLAB, yet FILMQA gave inaccurate results of profiles compared with the correction applied on MATLAB.

ABRÉGÉ

Délivrer un traitement conforme à la planification est une des responsabilités du physicien médical; ceci est relativement simple à vérifier en Radiothérapie Conformationnelle. Cependant, la complexité des calculs en Radiothérapie avec Modulation d'Intensité (RTMI) rend cette vérification moins évidente puisque la relation entre la dose et les unités moniteures est plus difficile à établir. En conséquence, irradier un fantôme conformément au plan établi pour le patient est une étape effectuée avant chaque traitement. Cette irradiation s'accompagne d'une mesure à l'aide d'une chambre d'ionisation et d'une mesure des distributions de doses à 2D. Dans cette thèse trois points sont soulevés. Le premier consiste à évaluer le Computed Radiography (CR) en dosimétrie; le protocole proposé a mené à une réponse linéaire mais dépendante en énergie et en largeur de champ. En second lieu, une comparaison de deux films (EDR2 et EBT) largement utilisés pour l'assurance qualité en RTMI a été effectuée. L'étude a montré qu'en dose relative, EDR2 donnent de meilleurs résultats que EBT. Ceci est attribuable au fait que le contraste enregistré avec EDR2 rend les artefacts de scanners moins importants sur le calcul de dose comparativement à EBT. La troisième partie de ce travail traite de l'importance des artefacts introduits lors de la lecture des EBT sur le scanner EPSON1680. Une correction de ces artefacts, effectuée sur MATLAB, a prouvé leur importance. Le logiciel FILMQA utilisé en clinique pour le traitement des films a montré une grande erreur sur la mesure des profils, mais sur 15 plans d'RTMI étudiés, un seul cas a véritablement été amélioré par la correction effectuée sur MATLAB.

Chapter 1: INTRODUCTION

1.1 INTRODUCTION TO RADIATION THERAPY

The history of Radiation Physics started on Friday, November 8th, 1895, when German physicist Wilhelm Conrad Roentgen discovered X-rays[1]. Shortly after, on December 22nd 1895, he took the famous first X-ray image of his wife’s hand, shown in Fig. 1.1[2].

Figure 1.1: First medical X-ray image,
of the hand of Anna Berthe Roentgen[2].

The next step occurred in 1896 when the Frenchman Antoine Henri Becquerel was checking for the possibility that the newly discovered X-rays might also induce fluorescence on uranium salts. Becquerel noticed that the photographic plate in which the potassium uranyl sulfate was wrapped had darkened before he shot the X-rays; thus, natural radioactivity was discovered[3]. For her thesis, the

Polish Maria Skłodowska-Curie chose to study natural radioactivity in 1897 and discovered radium with her husband, Pierre Curie[3]. X-rays and radium found applications in medicine very quickly. The first successful treatment by ionizing radiation modality (applied on a basal cell carcinoma), appeared in the literature in 1899[4]. In the U.S., William Coolidge introduced the ductile tungsten filament to X-ray tubes in 1913, which enabled the production of photons up to the energy 200 keV in 1922[3, 4]. The X-ray tube is still used for superficial lesions because of the high surface dose and low penetration of kilovoltage photons; however, betatrons went into service in clinics, at the end of the Second World War, in order to treat deeper targets. The betatron was developed in the U.S. by Donald Kerst in 1940[3]. In this machine, the electrons emitted from a filament are accelerated using an alternating magnetic field; electrons can produce megavoltage photons after impinging selected targets. The first betatron in Canada was built in 1948 at the University of Saskatchewan[5]; nine months later, it served to deliver the first treatment by betatron in the world[6]. In 1951, Harold Johns developed the Cobalt machine in Ontario[4] (shown in Fig. 1.2[7]).

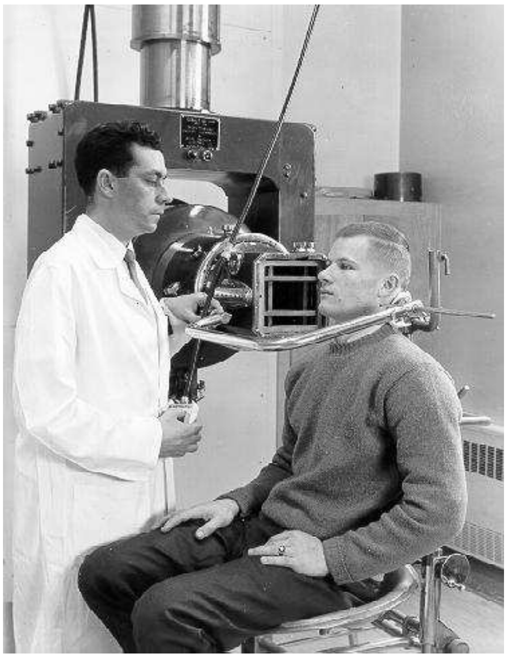

Figure 1.2: First Cobalt machine[7].

Cobalt is a radioactive source emitting at 1.17 MeV and 1.33 MeV. Cobalt machines have remained important even after the introduction of the first linear accelerator in the early 1950s in London[4]; this machine produced 8 MV X-rays and treated the first patient in 1953. The first linear accelerator (linac) in Canada went into service in 1964 in Saskatchewan[6]. Linacs are the most widely used modality for cancer treatment in industrialized countries; they can be isocentrically mounted and offer a higher output compared to betatrons. Currently, radiation therapy, surgery, and chemotherapy, used individually or in combination, are the three main methods of fighting cancer. Surgery consists of removing the affected organ, while chemotherapy combines different drugs that attack the DNA of cancerous cells. Like chemotherapy, the objective of radiation therapy is also to damage the DNA of cancerous cells. However, in such treatment, healthy tissues are never completely spared. A major challenge of radiation techniques is to limit damage by using the most conformal treatment, one in which the dose distribution will match the tumour shape as well as possible and spare healthy organs, as much as possible. This issue also became possible with the introduction of computed tomography (CT), introduced in 1972 by the English Godfrey Hounsfield[2]. CT imaging procedures allow 3D visualization of tumours, and the calculation of 3D dose distributions. The development of this technology as well as magnetic resonance imaging (MRI) and positron emission tomography (PET) have allowed for the improvement of radiation treatment planning and delivery.

There are two types of radiation therapy procedures, external and internal radiotherapy. Internal radiotherapy (also referred to as brachytherapy, curietherapy or endocurie therapy) consists of inserting a small radioactive source close to or within the tumour; this technique is particularly effective when the tumour is of small size, well localized, and surgically accessible. For larger tumours, external radiotherapy utilizes sources of ionizing radiation that are outside the patient's body. These sources include kilovoltage radiation photons, obtained with X-ray tubes, megavoltage beams delivered by linear accelerators, which produce electrons or bremsstrahlung photons, or radio-isotope sources capable of delivering penetrating beams. Clinical photon beams are produced such that they are of relatively uniform intensity. Wedges, compensators positioned on the head of the gantry, or blocks positioned on the patient’s skin can be used to modify intensities in order to spare healthy tissues, or to have a more conformal dose distribution. The combination of CT based planning with multifield beam delivery, in which the dedicated dose is conformal to the target, is known as 3D conformal radiotherapy (3DCRT)[4]. The need for a large number of beams is one of the downsides in 3DCRT when the aim is to avoid irradiating sensitive areas, such as the bladder and the rectum for prostate cancer, or the spinal cord and the salivary glands in head and neck cancer cases. It is also difficult to achieve dose conformity for concave tumour shapes. The event of intensity modulated radiotherapy have corrected for some limitations of 3DCRT.

1.2 INTENSITY MODULATED RADIATION THERAPY

Intensity Modulated Radiation Therapy (IMRT) refers to the delivery of photons of a non uniform intensity[8] over the target to optimize dose distribution while sparing organs at risk. Wedges, compensators, transmission blocks and dynamic jaws used in 3DCRT can achieve that goal; nonetheless, IMRT uses devices that allow non uniform and very complex dose distributions, such as concavities, that are difficult to obtain with standard equipment. A report published in 2001 by the Intensity Modulated Radiation Therapy Collaborative Working Group (CWG) [9], cited five different IMRT delivery techniques. These include scanned beam IMRT, tomotherapy, Physical modulators, robotic linacs and IMRT with the multileaf collimator. Scanned beam IMRT consists of focusing the electron beam to a desired angle when impinging the target to create photons; these can be placed to any position into the field using a scan pattern that provides beam locations and intensities. This technique was the first published IMRT technique, but it suffered from limited resolution. Tomotherapy, which means slice therapy, is a radiation technique that uses a narrow slit beam and delivers IMRT by the same way as CT is performed. The use of physical modulators (or compensating filters) is a cumbersome method even if it provides good resolution and simple quality assurance. Robotic linear accelerator IMRT (ex. CyberKnife) consists of a small accelerator mounted on a robot, and used for small fields. Finally, the last and most widely used technology for IMRT delivery is the multileaf collimator. There are two important components related to the most common form of IMRT: inverse treatment planning, first published in 1988[10], and the multileaf collimators.

1.2.1 FORWARD VERSUS INVERSE TREATMENT PLANNING

In a 3DCRT treatment planning system (TPS), the planner chooses the number, direction and field size of the beam, and selects blocks or wedges as well as the prescription dose. The computer uses a combination of a beam model and measured data in order to simulate a treatment on the acquired images (generally CT images). If the evaluation of the dose distribution is satisfactory, the treatment plan will be delivered; otherwise, another beam configuration will be tried. This is known as the forward planning method. However, it was shown that IMRT treatment plans can be improved by the inverse treatment planning process[11]. In the inverse TPS, the planner uses a number of fields and enters the planning constraints, namely, the dose prescription with the maximum and minimum acceptable dose for healthy tissues. Following these constraints, the TPS determines the non uniform beam intensities required by each beam to determine the best trade-off between the desired delivery to the target and minimum fluence over organs at risk. For example, Fig 1.3 shows nine intensity maps calculated by the inverse TPS[9]. After determining the photon intensity maps, TPS calculates the dose.

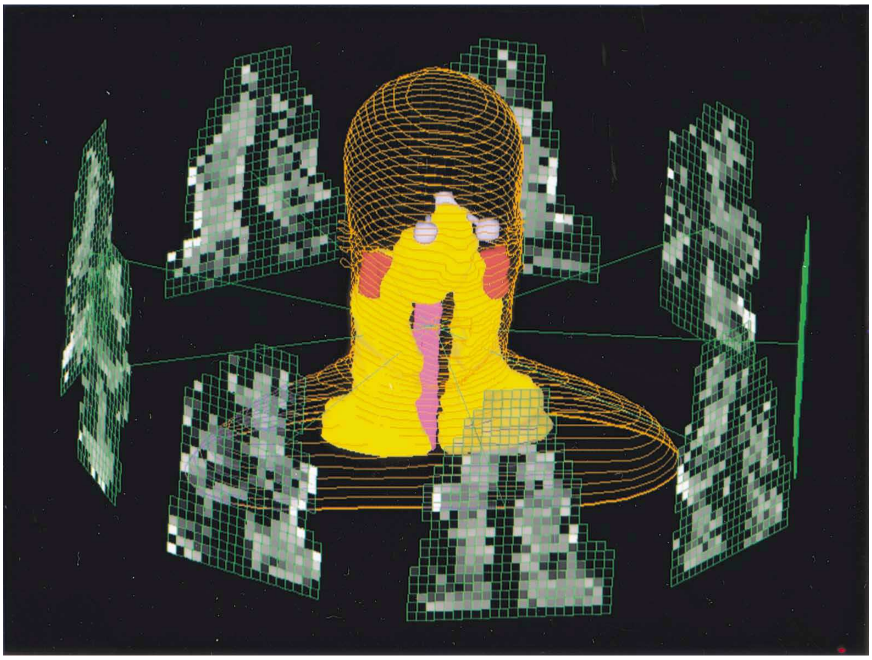

Figure 1.3: 3D images are used by the inverse TPS to acquire nine intensity maps. Each intensity map will be delivered by motorized MLC[9].

1.2.2 IMRT TREATMENT DELIVERY USING MLC

The first MLC was invented and patented in 1959[10]; however, it did not become standard equipment on linacs until the early 1990s. MLC is a device made of tungsten alloy (shown in the Fig 4.2). MLC is positioned in the gantry head, after the lower jaws, and composed of pairs of leaves that move in the same direction according to the desired shape. There are three methods to deliver IMRT with MLC. In the multi-segment static fields method (also referred to as step and shoot), radiation is delivered with a uniform intensity once the leaves are shaped for a certain subfield. It is the superposition of many such subfields, for each gantry orientation, that create a non-uniform intensity. The beam is on until the MLC is in a fixed position, and is turned off between fields. The dynamic delivery method, also referred to as the sliding window, follows the same technique as the first; however, the beam remains on from one subfield to the other. The third method is arc therapy, where the beam is continuously on while the gantry is rotating, and the MLC changes shape to conform to the tumour. The advantage of dynamic IMRT compared to the static method resides on the shorter time delivery; however, precise quality assurance on MLC is more important during the dynamic delivery.

1.3 QUALITY ASSURANCE PROCEDURES FOR IMRT

Quality assurance (QA) consists of a set of tests dedicated to control and verify a standard of quality. In radiation therapy, QA is defined as all procedures that ensure consistency of the medical prescription, and safe fulfilment of that prescription, as regards the dose to the target volume, together with minimal dose to normal tissue, minimal exposure of the personnel, and adequate patient monitoring aimed at determining the end result of the treatment[12]. Particular QA procedures on equipment should follow a predetermined schedule, and should be performed daily, monthly, or annually. Important examples include checking that the variance of the isocenter position is within 2mm, that the field light and radiation field coincide within 2mm, and that MLC motion adequately follows its programming. The IMRT Subcommittee of the Radiation Therapy Committee released a report - Report #82 - which was published by the American Association of Physicists in Medicine (AAPM) in 2003[13]. The report provides recommendations on delivery, treatment planning and clinical implementation of IMRT as well as a variety of related references.

1.3.1 ROUTINE QA ON MLC

Multileaf collimators are made with tungsten alloy[14]. Each leaf is rounded, as shown in Fig 4.2, because flat leaves would create penumbra dependent on field size[15]. A minimum distance between opposite leaves is required to avoid leave collision. Adjacent leaves are designed with a ‘tongue-and-groove’ arrangement in order to minimize interleaf transmission[16]. The offset between the light and radiation field is important for MLC calibration. In 2000, a publication stated that uncertainty on the offset can produce up to 20% deviation on delivered dose per millimetre offset in a 1cm leaf width[17]. This large deviation makes quality assurance on the MLC function very important in IMRT delivery. For example, the picket fence test consists of driving the leaves to a certain position, so that the irradiation shape looks like a picket fence; any discrepancy on leaf position will appear on the image obtained on a film. Introduction of intentional errors on leave positions, in millimetre range, is known as the acceleration test. The skew test aims for verifying that MLC motion is parallel to the jaws.

1.3.2 PATIENT SPECIFIC QA AND ITS RATIONALE

IMRT dose calculations are performed by algorithms that provide optimal MLC shapes for the different beamlets (subfields of the total field) as well as the number of monitor units to be delivered for each beam. However, IMRT algorithm calculation is complicated; therefore it is impossible to make a manual verification for the number of the calculated monitor units. Available software programs based on the Clarkson method represent an alternative[18], but the most widely used method for IMRT treatment verification is to perform patient-specific quality assurance measurements[19]. The lack of charged particle equilibrium in some portions of IMRT fields violates the Bragg Gray cavity theory. This creates uncertainties on dose assessment by using an ionization chamber[20], so that ionization chambers must be used in a uniform dose region in IMRT. Patient-specific quality assurance involves irradiating a phantom with the fields planned for the patient, performing an ionization chamber reading in a uniform dose distribution region, and carrying out a film measurement to acquire a 2D dose distribution. If measurements on the phantom agree with the simulation on the phantom, we assume that the patient delivery will agree with the treatment plan.

1.4 THESIS OBJECTIVE

There are three aims in this project. The first is evaluating the photostimulable phosphors (also known as computer radiography or CR) for dosimetry in megavoltage beams, and particularly for 2D IMRT planar dose distributions. The second objective is to compare two widely used films in IMRT QA, namely, the radiological film EDR2 and the radiochromic film EBT. Thirdly, this thesis aims to study the impact of scanner artifacts on dose assessment with EBT films and the EPSON1680 scanner.

Chapter 2: THEORY

2.1 INTERACTIONS OF PHOTONS WITH MATTER

When an initial number (N_0) of mono-energetic photons enter in a medium, some of them are absorbed; however, photons that escape without interacting with the medium don't change their trajectory. Their number (N) is given by the following equation[21]:

$$N = N_0 \exp(-\mu x) \quad (2.1)$$

In this equation, (μ) is the linear attenuation coefficient given in (cm^{-1}), which is related to the probability of photon interaction, and (x) represents the thickness of the medium in (cm). There are three main interactions of photons with matter: photoelectric effect, Compton effect and pair production. Each of these processes has its own linear attenuation coefficient, and the coefficient (μ) in the equation (2.1) is actually the sum of all the attenuation coefficients relative to each interaction. The mass attenuation coefficient $\left(\frac{\mu}{\rho}\right)$ is defined as the ratio between the linear attenuation coefficient and the density of the absorber (ρ).

2.1.1 PHOTOELECTRIC EFFECT

A photon undergoes photoelectric effect (also referred to as photoeffect) with tightly bound orbital electrons[21]. The result of photoelectric effect is the total absorption of the photon by the electron (referred to as the photoelectron) that is emitted with a kinetic energy $(E_K = h\nu - E_B)$; $(h\nu)$ is the incident photon energy and (E_B) is the binding energy of the electron. Important aspects of the photoeffect include the dependence of its mass attenuation coefficient $\left(\frac{\mu}{\rho}\right)_{Photoeffect}$ on the square of the atomic number (Z) of the absorber, and its rapid decrease with energy, as shown in Fig 2.1.

2.1.2 COMPTON EFFECT

A photon of energy $(h\nu)$ undergoes the Compton effect (also referred to as Compton scattering) by transferring part of its energy to a loosely bound orbital electron[21]. This results in a scattered photon of energy $(h\nu')$ and an electron (also referred to as Compton electron or recoil electron) that is ejected with a kinetic energy equal to $(E_K = h\nu - h\nu')$. Important aspects of the Compton effect are the independence of its mass attenuation coefficient $\left(\frac{\mu}{\rho}\right)_{Compton}$ on the atomic number of the absorber, and its decrease with energy, as shown in Fig 2.1. If a Compton effect occurs without any transfer of energy, then it is not important in dosimetry; this is referred to as Rayleigh scattering, an interaction that involves the whole atom and not a particular electron.

2.1.3 PAIR PRODUCTION

If a photon passes in the vicinity of a nucleus, with an energy higher than the threshold of 1.022MeV, it can be annihilated, and its entire energy is converted to the creation of a positron-electron pair[22]. Due to the short half-life of the positron, pair production is followed by the annihilation of the electron-positron pair, which then results in the emission of two photons of 511 keV emitted at

180^0 to each other. Mass attenuation coefficient of pair production $\left(\frac{\mu}{\rho}\right)_{PP}$ is proportional to the atomic number (Z).

2.1.4 INTERACTION COEFIECIENTS

The mass attenuation coefficient of the Compton effect, photoeffect, and pair production (PP) in water and silver halide (AgBr) are plotted in Fig 2.1[23]. It shows that the Compton effect probability increases for very low energy photons and decreases again with energy. The first observation about the photoeffect is its dominance at low energies and its rapid decreasing with energy. Photoeffect mass attenuation coefficient of (AgBr) displays peaks (referred to as absorption edges) that correspond to the binding energy of K, L, or M electron shells.

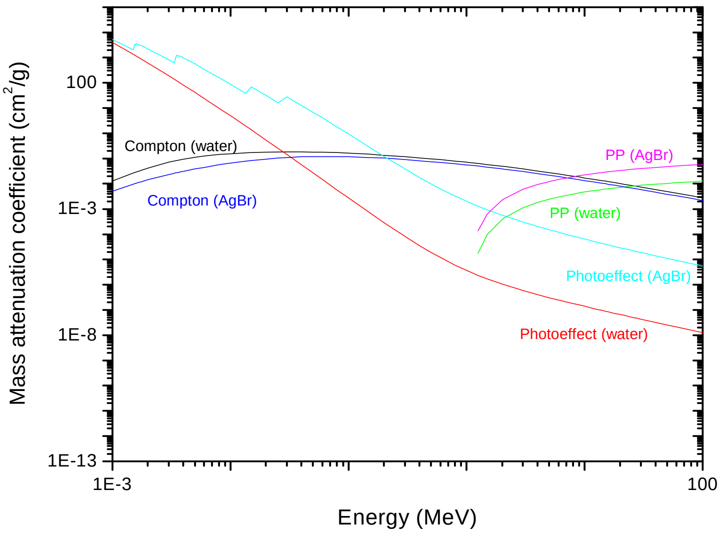

Figure 2.1: Mass attenuation coefficient of the Compton effect, photoeffect, and pair production (PP) in water and silver halide (AgBr)[23].

The photoeffect mass attenuation coefficient in silver halide is higher than that in water because of its dependence on the square of the atomic number. Pair production starts to occur at the threshold of 1.022 MeV, and increases again with energy. The pair production mass attenuation coefficient in silver halide is higher than that in water because of its dependence on the atomic number.

In addition to these three important interactions, there are two other interactions of photons with matter that are important at very high energies. Triplet production happens if a photon with energy higher than 2.044 MeV passes in the vicinity of an orbital electron; the photon energy is completely converted to create a positron and an electron, and the orbital electron is ejected from its shell. The mass attenuation coefficient of triplet production is proportional to the atomic number (Z). The second interaction is the photonuclear reaction. It happens when an energetic photon with an energy level higher than 8 MeV - the mean binding energy of neutrons and protons - is absorbed by a nucleus. This leads to the emission of a neutron[3]. In photonuclear interactions, the daughter nucleus generated by the (γ, n) reaction can be radioactive. Neutrons can also interact with air, creating radioactive oxygen and nitrogen; this requires adequate ventilation in the treatment room. Photon interaction with a medium is a stochastic event; every interaction is determined by a probability distribution. Since the dose is a non-stochastic quantity that is determined from photon interactions, it is important to know the dominance of each interaction with an absorber for a given energy photon. Figure 2.2 summarises the regions of relative dominance of photon interactions with absorbers[3]. Figure 2.2 shows that the photoeffect is the dominant process at low energy while the Compton effect is dominant for megavoltage photon beams. Pair production starts to happen at 1.022 MeV photon energy. For high atomic number materials, pair production is the major photon interaction at 4 MeV, whereas higher photon energies are required for its dominance in lower atomic number absorbers. In water, photoeffect is dominant up to 30 keV in contrast to 220 keV in AgBr; the Compton effect remains important in water up to 26 MeV in contrast to 7 MeV in AgBr.

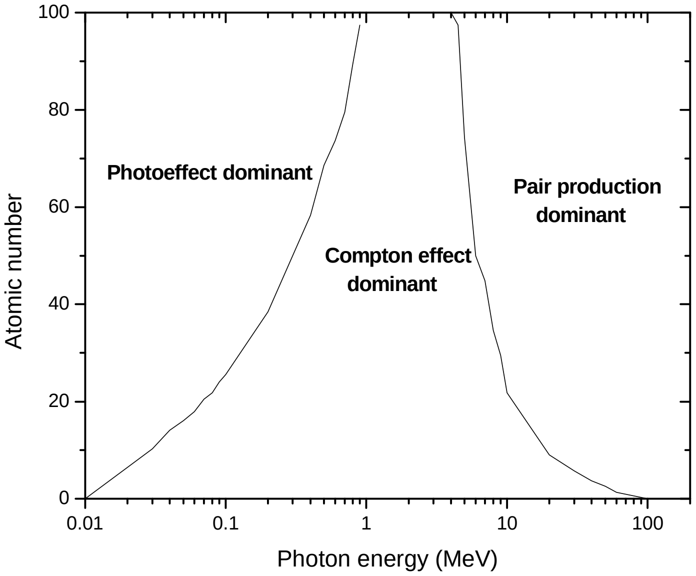

Figure 2.2: Regions of relative dominance of photon interactions with mediums[3].

2.2 INTERACTIONS OF ELECTRONS WITH MATTER

Electrons deposit the dose in the medium by interacting with electrons or nuclei; they are considered as directly ionizing radiation. If (dE) is the electron kinetic energy loss in an infinitesimal linear thickness (dx) in a medium of density (ρ), mass stopping power $\left(\frac{S}{\rho}\right)$ represents the rate of energy loss of the electron per unit of thickness, and density of the medium $\left(\frac{S}{\rho}=\frac{1}{\rho}\frac{dE}{dx}\right)$, expressed in $\left(MeV\,cm^2/g\right)$. Electron energy loss depends on its energy, as well as on its distance from orbital electrons or nuclei so that $\left(\frac{S}{\rho}\right)$ is divided into two components: collisional stopping power and radiative stopping power.

2.2.1 COLLISION INTERACTIONS

Incident electrons interact with orbital electrons leading to excitation or ionization. The loss of electron energy by interacting with orbital electrons is referred to as mass collision stopping power $\left(\frac{S}{\rho}\right)_{Coll}$. The minimum energy transfer from an incident electron to an orbital electron is the mean ionization energy, and the maximum is half the incident electron energy.

2.2.2 RADIATIVE INTERACTIONS

The loss of electron energy due to interactions with nuclei, leading to photon emission, is known as mass radiative stopping power $\left(\frac{S}{\rho}\right)_{Radl}$. This electron interaction leads to highly curved electron trajectories, and the emission of bremsstrahlung photons. Bremsstrahlung photon intensity is emitted in the forward direction for high electron energies[3]. This explains the parallel position of the patient in respect to the target in megavoltage radiation therapy. In contrast, the maximum intensity of bremsstrahlung photons in the kilovoltage range occurs at 90^0 thus, the patient is positioned perpendicular to the electron trajectory in diagnostic imaging.

2.2.3 ELECTRON STOPPING POWER

Mass collision and mass radiative stopping power of electrons in water and silver halide (AgBr) are plotted in Fig 2.3[24].

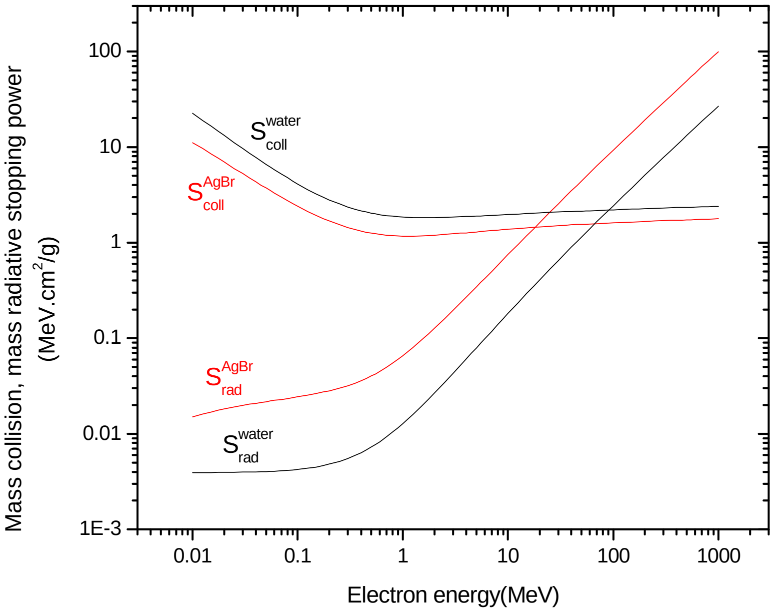

Figure 2.3: Collision and radiative stopping power of electrons in water and silver halide (AgBr)[24].

Figure 2.3 shows that the mass collision stopping power decreases rapidly with increasing electron energy due to the inverse proportionality between the intensity of coulomb interaction and electron velocity; the variation is then slower due to relativistic effects. Mass radiative stopping power increases with energy. Moreover, due to the dependence of bremsstrahlung production on the atomic number, $\left(\frac{S}{\rho}\right)_{Rad}$ is higher in (AgBr) than in water.

2.3 CHARACTERISTIC RADIATION AND AUGER EFFECT

An electron in a higher atomic shell fills a vacancy created in an ionized atom. The difference of its binding energy between the initial and final shell is emitted through two competitive processes[3]. This consists of a photon emission (or characteristic radiation) that obeys selection rules. If the selection rules forbid this emission, the Auger effect occurs; in this case, the energy difference is transferred to an electron from the same atom, which will be ejected. The Auger effect is the dominant process in elements that have an atomic number below 10 (such as water)[22].

2.4 KERMA AND DOSE

Electrons, or any charged particle, are referred to as directly ionizing radiation[3] while photons are considered to be indirectly ionizing radiation. A photon transfers kinetic energy to electrons, and this kinetic energy per unit of mass is referred to as kerma[22]. A portion of this transferred energy can be transformed into a radiative emission via bremsstrahlung interactions, or pair and triplet production. Such an event leads to the annihilation of positrons and the creation of photons. This energy per unit of mass is known as the radiative kerma. The rest of the transferred energy that is purely kinetic is referred to as the collisional kerma. Charged particle equilibrium is reached in the volume of a medium, when the number of electrons of a given energy that enter this volume is equal to the number of electrons of the same energy that leave it. In such a case, the dose inside the volume is defined as the collisional kerma. The Gray is the unit of kerma and dose, it corresponds to 1 Joule/kg.

Chapter 3: FILM AND COMPUTED RADIOGRAPHY DOSIMETRY

A radiation dosimeter is a device that measures, directly or indirectly, the dose in a certain medium[12]. Dosimetry system refers to the device with its reader; for example, if the ionization chamber is the device, the electrometer is the reader. A desirable dosimetry system must have characteristics such as accuracy, precision, linearity, dose rate independence, directional independence and good spatial resolution. Calorimeters are known to be absolute dosimeters; they measure the increase of temperature that is directly related to deposited dose. Fricke dosimetery is a chemical dosimetry system that uses the induced ionization to evaluate the dose. This process involves the determination of ionization energy (referred to as the G value), which is not an easy task. Thermoluminescent dosimeters (TLD’s) are made of phosphorescent materials that emit light upon exposure to radiation; they are interesting for invivo dosimetry, but they have cumbersome readout techniques. Indeed, TLD’s must be heated before and after the reading and their calibration is time consuming. Diodes have the advantage of being a simple device for dosimetry and exhibit a high sensitivity. They are often used for electron dosimetry because of the independence of the ratio of stopping power silicon to that of water with energy. The ionization chamber is the most commonly used dosimeter in clinics because it is robust, easy and fast to use. However, all these mentioned dosimeters have limited spatial resolution, and this is an important characteristic in intensity modulated beams where the dose distributions exhibit nonuniformities and high dose gradients. For this reason films are an ideal detector for 2D dosimetry, particularly for IMRT quality assurance.

3.1 FILM DOSIMETRY

3.1.1 RADIOGRAPHIC FILMS

Films have played an important role in imaging for a long time; nowadays, their application is more important in radiation therapy than imaging because the Computed Radiography is the ideal instrument for digital archiving images[2]. The sensitive layer of a radiological film consists of an emulsion of grains of silver halide distributed in a gelatine layer[1] . The base, made with Polyester[2], serves as a support to the fragile emulsion on one side and the coating protects the second side of the emulsion from possible damage. The first commercialized films contained one emulsion; currently, double emulsion is used for its fast response to radiation as shown in Fig 3.1.

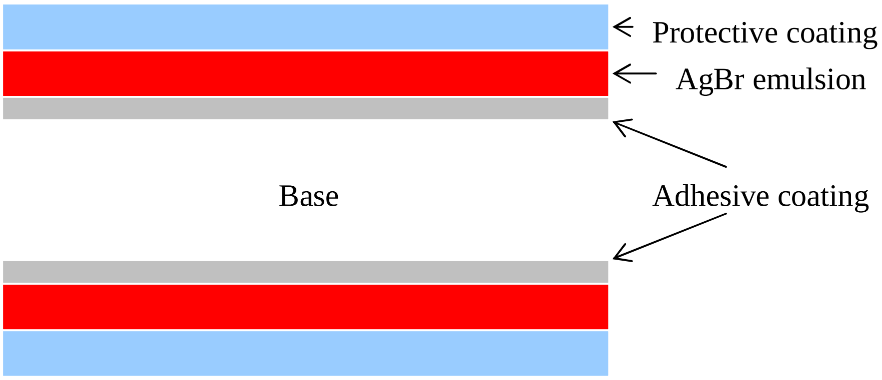

Figure 3.1: Composition of a double sided radiological film.

3.1.1.1 THE LATENT IMAGE

The widely accepted theory about the formation of the latent image in films is the Gurney and Mott mechanism[25, 26]. Each silver halide grain contains defects in its lattice structure, made by the introduction of silver sulfide (AgS)[2], that defines the optical characteristics of the grain. This region of defect is called a speck. When the silver halide is exposed to radiation, the ions undergo oxidation following the equation: $Br^{-} + irradiation \rightarrow Br + e^{-}$. Released electrons are attracted to the speck of the grain; as a result, the positive silver ions are pushed to the speck where they are reduced; thus, the latent image is formed. A grain contains about 10^{10} silver ions, but only few of them will constitute the latent image. Since this latter is not visible, a development process is required to obtain the definitive image.

3.1.1.2 FILM PROCESSING

During the processing, the film passes through different baths of the processing machine: The developer, the fixer, the washer baths and finally the dryer. In the developer, the film is put in an acid chemical solution called the developer: The few silver atoms (Ag) present in the speck are the catalyst to spread the reduction of all silver ions Ag^{+} present in the grain; thus, the film becomes darker due to the formation of metallic silver in the grains that were irradiated. In theory, all silver halide grains where the specks have not been reached by the silver ions Ag^{+} remain insensitive to the chemical developer. In reality some of them are developed, producing the so called Fog. The actual resolution of a film is not the dimension of the speck, but the dimension of the grain, which is specific to each kind of film. The fixer is a basic solution that aims to stop the development process done in the first bath. After the process of fixation, the film passes through a bath of water for rinsing and is finally dried with heated air by a powerful fan.

Extended Dose Range EDR2 films were introduced by Kodak Eastman Company in 2001[27]. EDR2 were commercialized to correct for the low dynamic range of the previously used XV films. For comparison, the physical characteristics of XV and EDR2 are summarized in Table 3.1[28]. Regarding the importance of EDR2, the AAPM published, in 2007, the report of Task group TG-69. This latter provides guidelines for processing, scanning, and interpretation to accurately and precisely measure the dose with radiological films[25].

Table 3.1: Physical properties of EDR2 and XV films[28].

	EDR2	**XV**
Grain crystal	AgBr	AgBr and AgI
Total silver density $\left(g/m^2\right)$	2.303	4.237
Effective dimension (μm)	0.2	0.4
Grain size distribution	Monodisperse	Variation in shape and size
Base thickness (μm)	0.18	0.18
Cellulose coating thickness $\left(g/m^2\right)$	5	3
Double sided	Yes	Yes

3.1.2 RADIOCHROMIC FILMS

Radiographic films present the downside of being energy dependent; this is not the case of radiochromic film[29]. McLaughlin (from the National Institute of Standards and Technology, NIST) is credited to be the first who had studied radiochromic media in the 1960’s[30]. According to Soares, the interest in radiochromic film dosimetry dated to the mid 1980’s with the development of the first GAFchromic film by Lewis[31]. The importance of radiochromic films has lead to the publication of the AAPM radiation therapy task group TG-55 in 1999; it gives recommendations for the use of radiochromic films in dosimetry[30]. The sensitive layer of radiochromic films is composed of low atomic number dyes that undergo polymerization after irradiation, leading to a direct blue coloration[8]. However, it is well established that the process of polymerization continues even after irradiation, this highlights the importance of the film calibration[32]. Radiochromic film has been widely used as high dose detector, such as for medical product sterilization or food irradiation[33]. Doping radiochromic films with a high atomic number material increases their sensitivity without seriously affecting the best feature of these films which is their energy independence[29]. Many kinds of radiochromic films have been introduced for medical applications, such as HD-810, XR-T or HS type radiochromic films[34]. EBT (External Beam Therapy) film, commercialized by International Special Products (ISP, New Jersey), was developed to correct the non uniformity of the MD55 radiochromic films that was about 15%[35]. EBT films find applications in brachytherapy[36] [37], and are widely used for IMRT treatment verification[38]. EBT is composed of two active layers, coated in polyester; it has the following atomic composition[39]: ${}^{1}_{1}H(39.7\%),{}^{16}_{8}O(16.2\%),{}^{14}_{7}N(1.1\%),{}^{7}_{3}Li(0.3\%),{}^{35}_{17}Cl(0.3\%)$, as shown if Fig 3.2. This composition leads to an equivalent atomic number of Z=7.175, which is close to the atomic number of water. Fig 3.3 shows absorbance sensitivity of EBT films for different doses when exposed to a 6 MV beam[40].

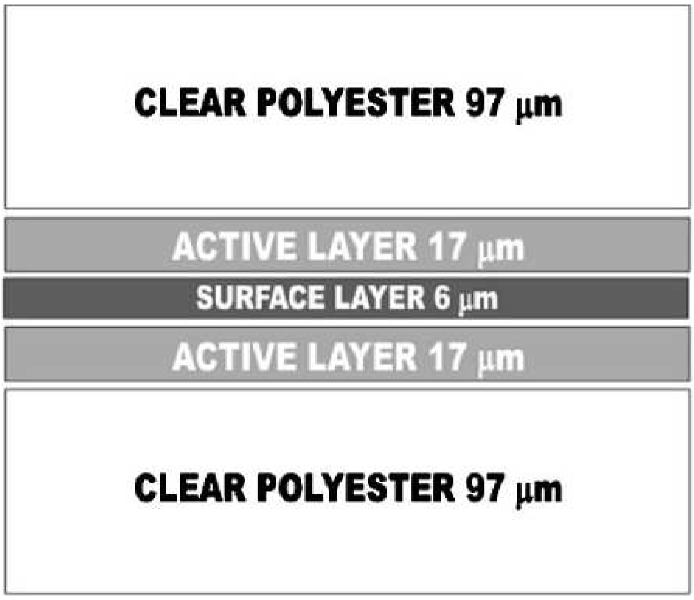

Figure 3.2: Composition of EBT radiochromic film[39].

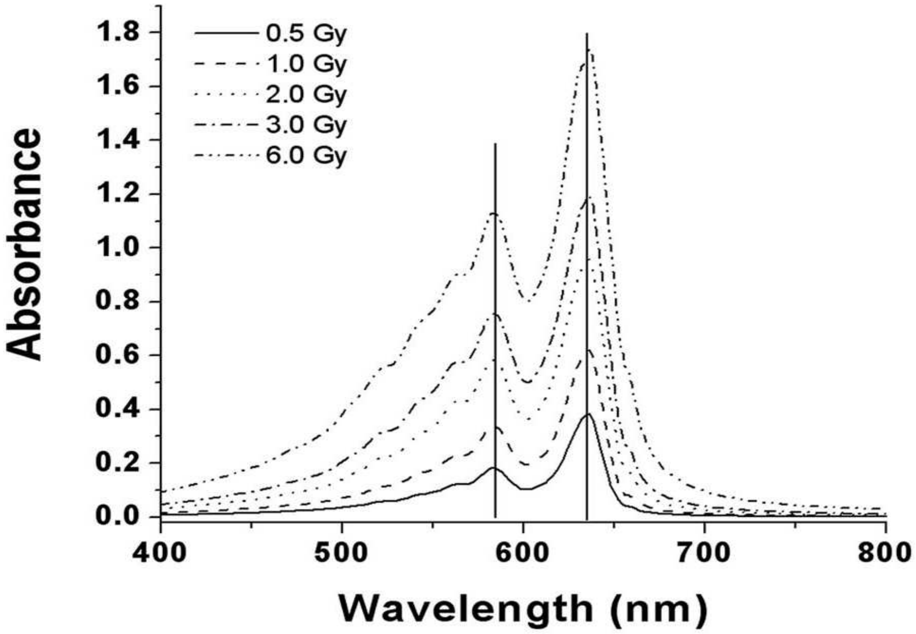

Figure 3.3: Net absorbance spectra of EBT radiochromic film at a 6 MV beam for different doses[40].

The shape of the spectrum in Fig 3.3 does not depend on the dose (up to 600 cGy); it exhibits a major peak at 635 nm, which is positioned in the red spectrum of visible light. This characteristic explains the use of the red channel when scanning EBT films. It should be noticed that polymerization is a chemical process that depend on temperature, so it is recommended to keep films at a constant temperature.

3.1.3 FILM CHARACTERIZATION

A dosimetric system must be understood as the ensemble of the device model, the readout and the measurement protocol[40]. In the case of film dosimetry, one should choose the kind of film, the densitometer (the scanner) and finally the calibration protocol.

3.1.3.1 OPTICAL DENSITY

Dose assessment is based on optical density or the pixel value (also referred to as scanner reading); both measurements quantify colour change on the film due to irradiation. Optical density (OD) is given by[25]:

$$OD = \log_{10}\left(\frac{PV}{PV_0}\right) \quad (3.1)$$

Where (PV) and (PV_0) are respectively the transmitted pixel value (or the scanner reading) measured in the absence and presence of the film.

3.1.3.2 SCANNER

Charged couple devices (CCD) are electronic devices used by scanners to create images of objects by transforming light to electrical signal such as with a photomultiplier tube but with a better sensitivity and spatial resolution. CCDs, shown in Fig 3.4, are made of metal oxide semiconductors; upon exposure to light, electrons travel from the valence band to the conduction band creating the captured image signal. Densitometers (scanners) can measure one line of pixel value by translating either the film or the light source and the (CCD) array perpendicular to the scan direction. Other scanners use a uniform light source and a 2D CCD camera to measure light transmission, avoiding then the need for translation. A linear CCD contains many CCD chips that are used in scanners; particular attention on the signal to noise ratio as well as the saturation of the scanner bed is then of great importance[41]. However, a significant characteristic of the scanners is the nonuniform light exposure; this leads to non uniform scanner response[42, 43]. Thus, any software used for dose assessment must carefully correct for scanner non uniformities .

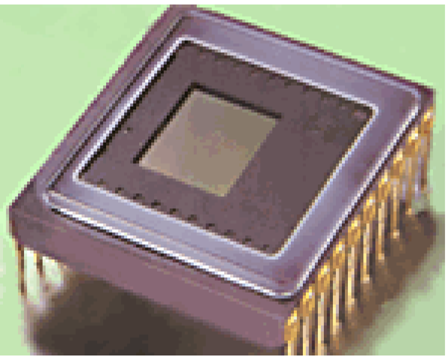

Figure 3.4: Chip of Charged Couple Device (CCD).

3.2 PHOTOSTIMULABLE PHOSPHORS

Phosphor means “light bearer” in greek[44], and photostimulable phosphor luminescence (PSL) effect is the storage of high incident energy radiation, which is released after photostimulation[45]. Some known applications of phosphors are fluorescent lamps and cathode-ray tubes. In medicine, they were used in X-ray screen to limit the delivered dose to patient during diagnostic because of the poor response of films to radiation. Phosphors can be used as thermoluminescent dosimeters (TLD) or scintillators in the $\gamma -$ ray camera, x-ray computed tomography detectors, or in positron emission tomography for imaging. Radiological films are being replaced by the Computed Radiography. Computed radiography, (CR) is the commercial name of the Photostimulable phosphor system[2] and is widely used in diagnostic radiology for digital archiving images.

3.2.1 CR PLATE

Phosphors are composed of a transparent microcrystalline host (the matrix) and an activator; the matrix in the case of CR imaging is the halide BaFBr which is doped with the europium activator Eu^{+}. $BaFX : Eu^{2+}$ where $\left(X = Cl, Br, I\right)$was discovered to be photostimulable in 1978; the first generation of CR system for medical diagnostic imaging was available in 1983[44]. $BaFBr : Eu^{2+}$ is the widely used material in CR because of its long image storing time where 75% of the signal can remain 8 hours after irradiation[46] and because of the best matching of its stimulation spectra with the wavelength of diode lasers used during the digitization.

3.2.2 CR LATENT IMAGE FORMATION AND DIGITIZATION

The latent Image formation in photostimulable phosphor material is complicated; it can be summarized, as shown in Fig 3.5, as the following[47] :

1- The activator is ionized due to the incident irradiation following the reaction: $Eu^{2+} + Irradiation \rightarrow Eu^{3+} + e^{-}$,and electrons are released to the conduction band.

2- The released electrons are trapped by the halogen ion vacancies, (which are called F^{+} centers) and the latent image is formed.

3- Photostimulation of F^{+} centers liberates electrons that are released again to the conduction band.

4- The released electrons in the conduction band are captured by Eu^{3+} inducing the photoluminescence of Europium. The intensity of photoluminescence is proportional to the incident irradiation.

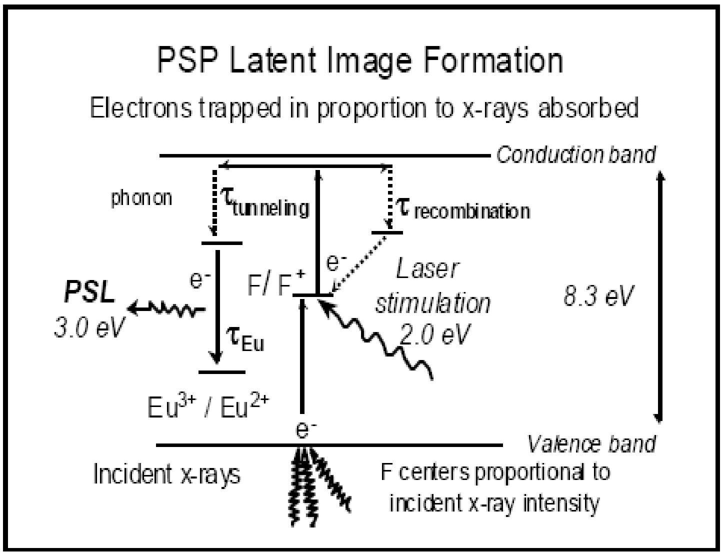

Figure 3.5: Formation mechanism of the latent image in Photostimulable Phosphor materials[45].

Figure 3.6 shows the digitization process. The plate is translated by rollers while the stimulation with a laser is performed leading to the photoluminescence. Emitted photons are guided to a photomultiplicator tube (PMT) that transforms photons to an electrical signal. This latter is digitized in the Analog to digital converter, (ADC). Immediately after digitization, the plate is erased by strong lamps.

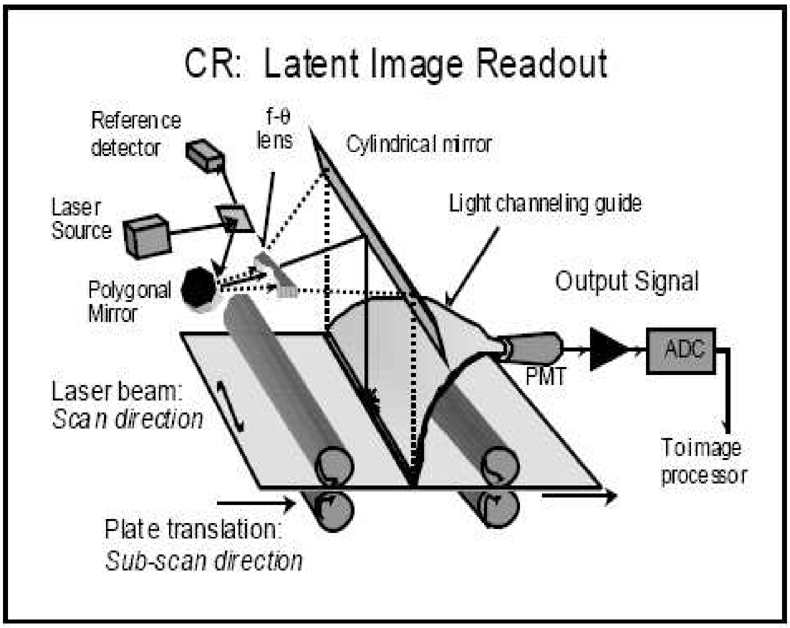

Figure 3.6: Digitization of the latent image in the Photostimulable Phosphor plate [45].

Chapter 4: MATERIALS AND METHODS

4.1 RADIATION DELIVERY

4.1.1 LINEAR ACCELERATOR AND CALIBRATION

The basic principle of a linear accelerator (Linac) involves the use of a disc loaded copper waveguide. This is shown in Fig 4.1[48]. Electrons are emitted from the gun, a super-heated tungsten filament, and are accelerated through the waveguide. The latter is polarized by a carefully synchronized injection of RF microwaves operating at 2856 MHz. Accelerated electrons reach the megavoltage energy range. They can be scattered (through scattering foils), or used to strike high atomic number targets to produce bremsstrahlung photons. The treatment beam (electrons or photons) passes through a primary collimator, a dose monitoring system, and the upper and lower jaws. Multileaf collimators are positioned after the lower jaws, and are used with photons. A Varian clinic 6EX Linac, capable of producing 6 MV photons, was used in this work. Linac's output was calibrated with an ionization chamber; this ionization chamber was calibrated based on the recommendations of Task Group TG-51[49], and positioned at a depth of 10 cm within a solid water phantom. Measurement was taken with a source to surface distance of 100 cm, and a $10*10cm^2$ field size. The output at maximum depth dose was obtained from the equation (4.3); the machine was calibrated at 1 cGy/MU in water.

Figure 4.1: Beam forming components of a linac[48].

4.1.2 MULTILEAF COLLIMATOR

The Varian multileaf collimators (MLC) used in this work are shown in Fig 4.2.

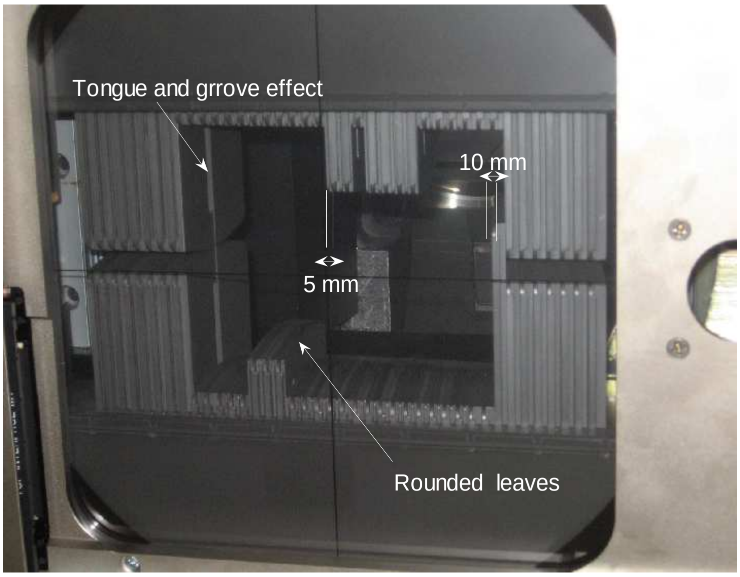

Figure 4.2: Pairs of Varian multileaf collimator.

The MLC consists of 120 leaves made of tungsten, and is able to produce an aperture with a field size of $40 * 40 cm^2$. Each leaf is rounded because flat leaves would create penumbra dependent on field size, while adjacent leaves are designed with a ‘tongue-and-groove’ arrangement in order to minimize interleaf transmission. The central 20 cm of the field is shaped by leaves measuring 5 mm in width, while the outer leaves are 10 mm wide; as shown in Fig 4.2.

4.2 PHANTOMS

The IMRT QA phantom used in this work is shown in Fig 4.3. It is composed of 3 rectangular slabs of solid water, GAMMEX Model 457 TM Material, with a mass density of $1.042\, g/cm^3$, and an electron density relative to water of 1.013. The three slabs have a surface of $30*30\, cm^2$, each one measuring 6 cm, 5 cm and 6 cm in thickness, respectively. The film is positioned at a depth of 6 cm, while an ionization chamber is placed at the centre of the second slab, at 2.5 cm from the film.

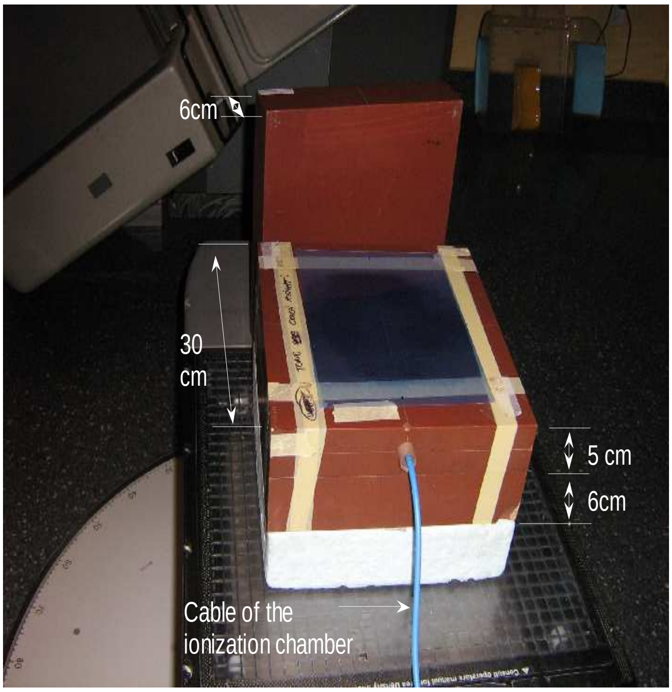

Figure 4.3: IMRT QA phantom.

4.3 DETECTORS

4.3.1 IONIZATION CHAMBER

A PTW FREIBURG 3000G ionization chamber was used; it was cross calibrated to clinical ionization chamber. The calibration factor, $(N_{D,w})$, expressed in cGy/nC, was used to measure the dose $\left(D(z)\right)$ at a depth equal to $\left(z\right)$ using the following equation:

$$D(z) = M(z) P_{T,P} N_{D,w} \quad (4.1)$$

$M(z)$ represents the charge reading at a depth equal to $\left(z\right)$, expressed in nC. $P_{T,P}$ is the factor that corrects for temperature $\left(T\right)$ and pressure $\left(P\right)$, since the volume inside the chamber is affected by these two environmental parameters. $P_{T,P}$ is obtained by the following equation:

$$P_{T,P} = \frac{760}{P(mmHg)} \frac{(273+T)^{0}}{295} \quad (4.2)$$

The correction for recombination, which depends on the voltage applied at the ionization chamber, was taken into account when the clinical ionization chamber was calibrated following the recommendations of Task Group TG-51 [49]. For output measurement, the chamber was positioned at a depth of $z = 10\,cm$. Maximum depth dose $(D(z_{\max}))$ is obtained by using the percentage depth dose at $z = 10\,cm$ as expressed in equation (4.3):

$$D(z_{\max)} = \frac{D(10cm)}{PDD(10cm)} \quad (4.3)$$

4.3.2 RADIOGRAPHIC EDR2 FILMS

Radiographic EDR2 films from Kodak (Eastman Kodak Company, Rochester, NY) were used in this project. EDR2 films were supplied in a box containing 50 films with $10*12\,inch^2$ ready pack envelopes (shown in Fig 4.4). Films from the same batch were used in this thesis.

Figure 4.4: EDR2 film in its envelope and an exposed EBT film.

4.3.3 RADIOCHROMIC EBT FILMS

Radiochromic EBT films from ISP (International Specialty Products, Wayne, NJ, USA) were used in this project. The films come in a box of 25 films, and each one measures $8*10\ inch^2$. Figure 4.4 shows an irradiated EBT film and an EDR2 in its envelope.

4.3.4 CR PLATE

In this project, a photostimulable phosphor system (referred to as computed radiography or CR) was evaluated for dosimetric purposes. A CR1.5 high dose was used as the CR system; it is a commercialized product from Agfa (Agfa Corporation, 275 North street, Teterboro, NJ, USA) that is designed for portal imaging. The active layer of the imaging plate (IP) measures 150 μm in thickness, and is composed of $(BaSrFBr:Eu)$ barium, strontium, fluorine, bromine and iodine; the IP is also doped with europium. The weight fraction of the plate, as provided by Agfa (in moles), is presented in Table 4.1.

Table 4.1: Weight fraction (in moles) of the CR1.5 high dose plate

Cations	Anions
Ba: 0.859	F: 0.05
Sr: 0.14	Br: 0.88
Eu: 0.001	I: 0.07

Taking into account the two dominant elements, Ba and Br, the equivalent atomic number of the active layer is $Z_{CR} = 50.35$. As shown in Fig 4.5, the IP is inside a cassette that contains 0.2 mm of tungsten. The tungsten, which has a high atomic number, $(Z_W = 74)$ aims to attenuate the scattered photons generated from the patient, as this leads to degrade the quality of the image.

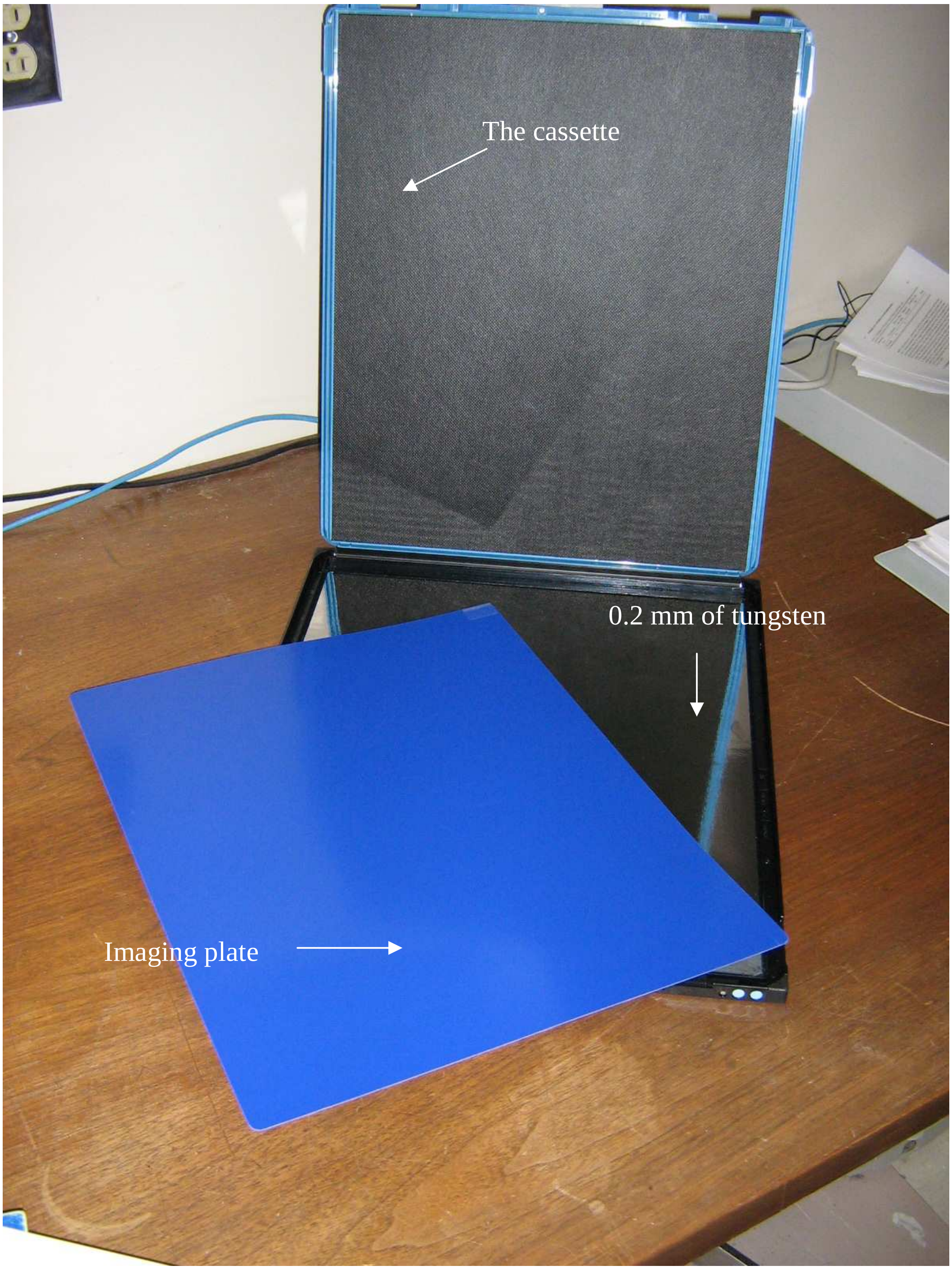

Figure 4.5: The CR imaging plate is kept in a cassette that contains 0.2 mm of tungsten.

4.4 DEVELOPERS AND READERS

4.4.1 FILM DEVELOPER

A Kodak RPX-OMAT processor, model M6B, was used as a film developer for this work. The temperature of the developer during processing was $T = (29.0 \pm 0.1)^{0} C$

4.4.2 EPSON SCANNER

An Epson Expression 1680 (Epson Seiko Corporation, Nagano, Japan) flatbed scanner was used in this project; it is shown in Fig 4.6. The scanner has a sensitive area of $11.68 * 8.5\ inch^{2}$, and employs a fluorescent light source with a broadband emission spectrum. This scanner is also able to operate in the transmission mode. Films were scanned in the RGB mode, where each colour was digitized in 16 bits.

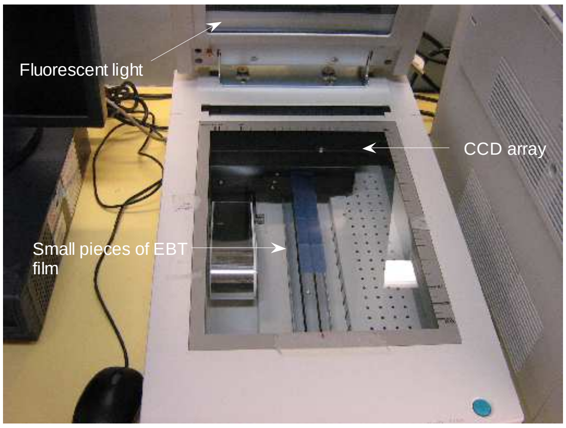

Figure 4.6: EPSON1680 flat bed scanner.

4.4.3 CR READER

The Agfa CR 25.0 digitizer is dedicated to digitize the CR1.5 high dose. As this CR reader was unavailable, an Agfa ADC solo was used instead for the digitization.

4.5 SOFTWARE

Two main software programs were used in this project. The first is the software FILMQA (3cognition LLC, a division of ISP), it is a commercially tool used in the clinic for IMRT QA. The software allows the calibration of the used film batch. This is done by scanning small exposed pieces of film in the center of the scanner; a calibration curve is plotted and saved. When a film is processed, FILMQA applies a background correction for each film by using the scan of an unexposed film. This correction normalizes signals to that obtained in the centre of the scanner; this is why pieces of film used to acquire calibration curves must be scanned in the centre of the scanner. Finally, FILMQA compares between simulation and measurement by three different methods: isodose comparison, γ index maps, and histograms of the γ index (the γ index will be defined later). The second software that was used in this work is MATLAB, version 7.0.4.365(R14).

4.6 CALIBRATION OF FILMS

Extended dose range (EDR2) and external beam therapy (EBT) radiochromic films were calibrated at 6MV in the perpendicular orientation. The calibration curve of EDR2 was performed by dividing each single EDR2 film (shown in the Fig 4.4) into six small pieces (shown in Fig 4.7); this took place in the dark room to protect the film from light exposure.

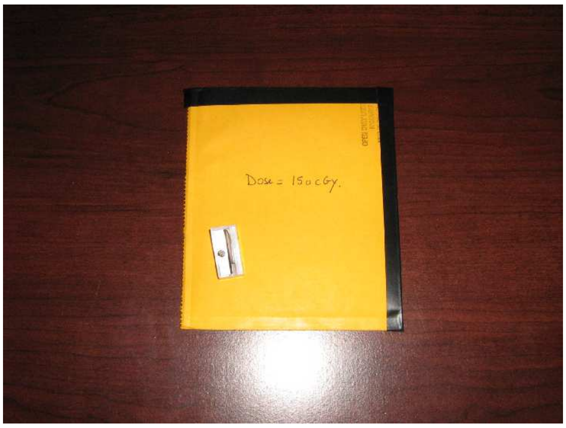

Figure 4.7: EDR2 films, cut and tipped to avoid light exposure.

EDR2 pieces were irradiated with an SAD setup at a depth of $z = 10\ cm$ and a field size of $A = 20 * 20\ cm^2$ for doses varying from 5 cGy to 1000 cGy. EDR2 films were developed 24 hours after irradiation. The number of monitor units relative to an SAD setup is calculated with the following equation:

$$MU = \frac{Dose(cGy)}{RDF(A,6MV)\,TMR(z,A,6MV)\,(1+\frac{1.5}{100})^2\,\dot{D}(cGy/MU)} \qquad (4.4)$$

RDF, TMR and $\dot{D}$ refer to the relative dose factor, tissue maximum ratio, and the dose rate or output of the machine. Each piece of EDR2 film exposed to a known dose was scanned at the center of the scanner bed following the manufacturer's recommendations on using FILMQA. The calibration of radiochromic films was performed by cutting unexposed EBT films (one EBT exposed is shown in Fig 4.4) into small pieces of $1*2\,inch^2$ (shown in Fig 4.6). The pieces were irradiated with an SSD setup at a depth of $z = 10\ cm$, and a field size of $30*30\,cm^2$ for doses varying from 10 cGy to 600 cGy. An ionization chamber reading was taken at a depth of $z = 12.5\,cm$ such that dose was carefully recalculated. Each piece of EBT film, which was irradiated with a known dose, was scanned at the centre of the scanner bed following manufacturer's recommendations for the use of FILMQA. The number of monitor units relative to an SSD setup was calculated with the following equation:

$$MU = \frac{Dose(cGy)}{PDD(z = 10\,cm, A = 30\,cm, 6MV, SSD = 100\,cm).\dot{D}(cGy/MU)} \quad (4.5)$$

4.7 CR EVALUATION

For the purpose of this study, the imaging plate (IP) was placed in a film envelope (in the dark) in order to protect the plate from light exposure, and was irradiated with the same procedure used for film dosimetry (the cassette was not used). Since it was not possible to use markers in the plate to define the position of the cross hairs, thin pieces of gold were taped to the envelope. Once the plate was irradiated in the solid water phantom, it was carefully inserted into the cassette (in the dark), and was digitized with the Agfa ADC solo. After each digitization, the IP is erased by strong fluorescent lamps. Because the digitizer was linked to software designed for diagnostic purposes, raw data were extracted from the ADC solo. With this digitizer, images have a format of 2 bytes per pixel; they are encoded in 2048 columns and 2494 rows, and the pixel size is 0.171 mm. In order to obtain the image, two readouts were registered; one digitization was performed before the exposure, and a second digitization was done after the exposure. The first step in assessing pixel value consisted in determining the sensitivity lookup table that corrects for possible non uniformities of the photomultiplicator tube (PMT). This process was performed as follows:

1- The IP was digitized before irradiation. The obtained image is referred to as the unirradiated image.

2- The IP was carefully inserted into a radiological film envelope; this process was done in the dark. The IP was placed at a depth of $z = 10\ cm$, in a solid water phantom measuring $30 * 30 cm^2$. The plate was exposed in a 6 MV beam, at a dose of 100 cGy, with an SAD setup and field size of $40 * 40 cm^2$. The choice of the field size is dictated by the aim of delivering a uniform dose, as recommended by Olch[50].

3- After exposure, the IP was carefully placed in a cassette (in the dark) and digitized. The obtained image is referred to as the irradiated image.

4- For analysis, the images were cropped to measure $20 * 20 cm^2$.

5- A Wiener filter was applied to raw data that were acquired in both the unirradiated and irradiated images. Thus, we obtained $PV_{irr,40*40}(i, j)$ and $PV_{unirr}(i, j)$, namely, the raw data at the pixel of coordinates (i, j) when the plate is irradiated with a field of $40 * 40 cm^2$, and the pixel value of the same point before irradiation. The mean pixel value $(\overline{m}_{irr,40*40})$ of the irradiated and cropped image, obtained for a field size of $40 * 40 cm^2$, was then calculated.

6- This step consisted of determining the sensitivity of each pixel. The lookup table for pixel sensitivity in the row (i) and column (j) was defined as:

$$LUT(i, j) = \frac{PV_{irr,4o*40}(i, j) - PV_{unirr}(i, j)}{\overline{m}_{irr,40*40}} \quad (4.6)$$

Once the pixel sensitivity lookup table was created, the pixel value in a point positioned at (i, j) was defined by:

$$PV(i, j) = \frac{PV_{irr}(i, j) - PV_{unirr}(i, j)}{LUT(i, j)} \quad (4.7)$$

In the equation (4.7), $PV_{irr}(i,j)$ and $PV_{unirr}(i,j)$ refer to the readout of the unirradiated and irradiated images, respectively, when both images have been cropped to measure $20*20\,cm^2$, and the Wiener filter has been applied.

4.8 GAMMA INDEX

Techniques that have been used to compare the measurement and calculation of 2D dose distribution for the commissioning of 3D treatment planning include the superimposition of isodose distributions for visual comparison, dose difference, and distance to agreement. Dose difference refers to the deviation between the measured and the calculated dose at the same point. On the other hand, distance to agreement is the closest distance between a measured dose point and the calculated dose distribution that receives the same dose. In 1993, Van Dyk published guidelines regarding the commissioning and quality assurance of treatment planning computers. He recommended a criterion of 3% dose difference and 4 mm distance to agreement for photon beams[51]. However, the dose difference and the distance to agreement criteria are two concepts that complement each other. For example, a small variation in space can lead to a high dose difference in regions of high dose gradient. A composite analysis was developed to show regions that fail both criteria of dose difference and distance to agreement; however this composite distribution is binary, and does not lend itself to interpretation[52]. This inconvenience led to the introduction of a more practical and restrictive technique, namely the γ index (gama index)[53]. In this method, every point from the measured distribution, defined by the vector $(\vec{r}_m)$ and the measured dose $(D_m(\vec{r}_m))$, belongs to a space that is composed of two spatial axes. The latter are relative to the 2D planar position. The third coordinate refers to the difference (δ) between the measured dose $(D_m(\vec{r}_m))$ and the calculated $(D_c(\vec{r}_c))$at a point defined by the vector$(\vec{r}_c)$.

The distance to agreement region is presented by a disc with a radius equal to (Δd_M), as shown in Fig 4.8.a[53].

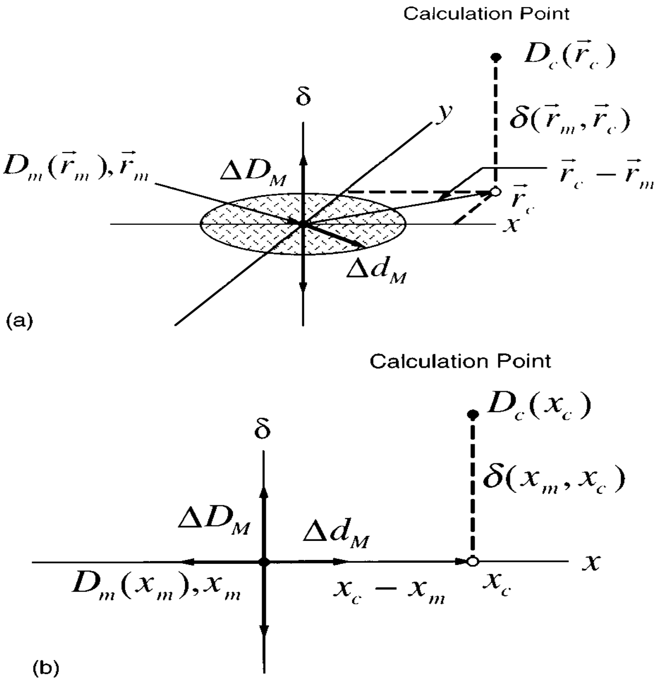

Figure 4.8: Geometric representation of the dose difference and the distance to agreement concepts in 2D (a) and 3D (b)[53].

In this dose-space domain, the measure of acceptability with the γ index forms an ellipsoid of equatorial radii, equals to the distance to agreement (Δd_M), and a polar radius, equals to the dose difference criterion (ΔD_M). Figure 4.9.a and

Fig 4.9.b show the geometrical representation of the dose distribution evaluation criteria using the combination of the ellipsoid dose difference, and the distance to agreement tests in 3D and 2D[53], respectively.

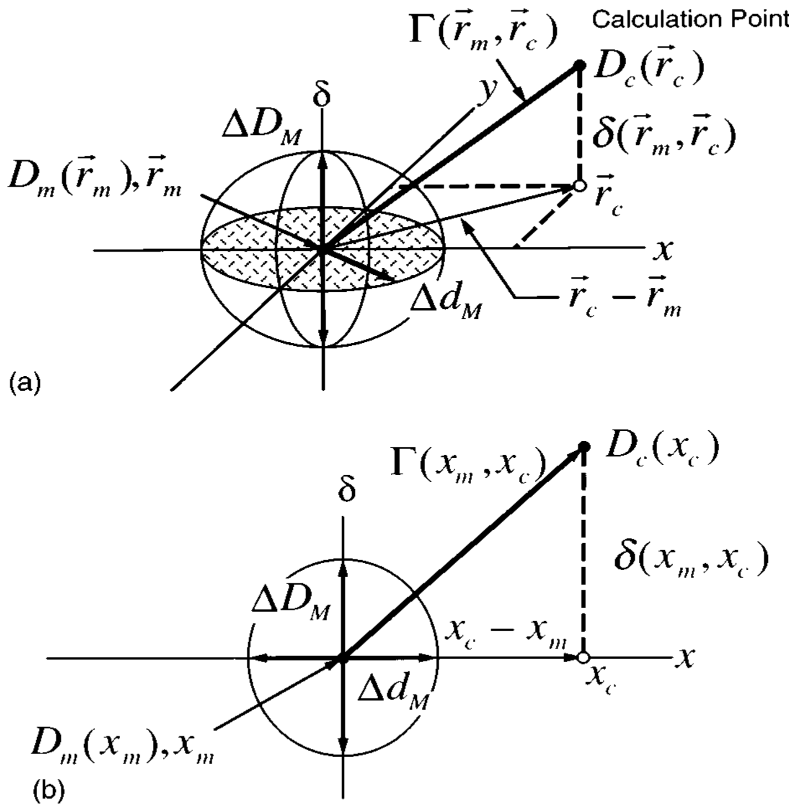

Figure 4.9: Geometric representation of the ellipsoid used with the γ index[53].

Quantitative evaluation of the γ index is performed as follows. If $(\vec{r})$is the vector position of a point in the calculated dose distribution where the dose is defined by $(D_c(\vec{r}))$, the equation (4.8) expresses the distance between this point and the point of coordinates $(\vec{r}_m)$ in the measured dose distribution with the dose $(D_m(\vec{r}_m))$.

$$r(\vec{r}_m,\vec{r}) = |\vec{r}_m - \vec{r}| \quad (4.8)$$

The dose difference is calculated with the equation (4.9):

$$\delta(\vec{r}_m,\vec{r}) = D_c(\vec{r}) - D_m(\vec{r}_m) \quad (4.9)$$

The surface that represents the acceptable criterion is the ellipsoid defined by the following equation:

$$\sqrt{\frac{r^2(\vec{r}_m,\vec{r})}{\Delta d_M^2}+\frac{\delta^2(\vec{r}_m,\vec{r})}{\Delta D_M^2}}=1 \quad (4.10)$$

The γ index at the point of coordinates $(\vec{r}_m)$ is defined by the following equation:

$$\gamma(\vec{r}_m)=\min\{\Gamma(\vec{r}_m,\vec{r}_c)\}\forall\{\vec{r}_c\} \quad (4.11)$$

$\Gamma(\vec{r}_m,\vec{r}_c)$ is calculated as such:

$$\Gamma(\vec{r}_m,\vec{r}_c)=\sqrt{\frac{r^2(\vec{r}_m,\vec{r}_c)}{\Delta d_M^2}+\frac{\delta(\vec{r}_m,\vec{r}_c)}{\Delta D_M^2}} \quad (4.12)$$

Finally, the pass/fail criteria of the point in the measured distribution are given in the equations (4.13) and (4.14), respectively.

$$\gamma(\vec{r}_m)\leq 1 \quad \text{The point passes the test} \qquad (4.13)$$

$$\gamma(\vec{r}_m)\geq 1 \quad \text{The point fails the test} \qquad (4.14)$$

J.R. Palta proposed different action levels concerning the used dose difference and the distance to agreement criteria for IMRT planning[54]. The acceptance criteria followed in this project were (3%, 3 mm) and (5%, 3 mm).

Chapter 5: RESULTS AND DISCUSSION

5.1 CR SYSTEM EVALUATION

The evaluation of a detector for dosimetric purposes must be performed by studying the dependence of the readout (pixel value for film dosimetry) on all these parameters:

1- Energy dependence
2- Field size dependence
3- Depth dependence
4- Dose rate dependence
5- Processing conditions
6- Detector orientation
7- Dose response (calibration curve)

The evaluation of a photostimulable phosphor device (CR) for dosimetry is dictated by some of these advantages: its digital function, its good resolution, its ability to display a wide dynamic range and a linear readout versus received doses. The linear behaviour and the reusability of the CR make it more attractive than films, where a calibration from one batch to another is required. So far, the literature review shows few publications on the use of CR in dosimetry, notwithstanding the introduction of the KODAK2000RT CR system for IMRT quality assurance by the Kodak Company in collaboration with RIT (Radiological Imaging Technology, 5065 List Drive, Colorado Spring, USA). The most important publication is a paper published by Olch in 2005; it is the only paper dedicated to the use of CR for megavoltage beams, and particularly for IMRT [50]. Two additional sources deal with this subject: a thesis authored by Jurkovic and submitted to the Louisiana State University[55], as well as two posters presented in 2007 during the 9^{th} Biennial Estro Meeting on Physics and Radiation

Technology for Clinical Radiotherapy[56, 57] . While the paper and the thesis concluded the real potential of CR in dosimetry, the two posters reported first measurements without giving a real conclusion. In this work, the verification of the CR behaviour consisted of, checking its response, its energy and field size dependence. Finally, a measurement of enhanced dynamic wedge was performed.

5.1.1 CALIBRATION CURVE

The irradiation of the plate was performed in a solid water phantom at a depth of $(z = 10cm)$, for a field size of $(10 * 10cm^2)$, and for dose exposures ranging from 5 cGy to 700 cGy. The readout was obtained by following the protocol presented in section 4.7. Figure 5.1 shows the calibration curve of the Agfa CR1.5 high dose used in this study. Pixel values of the CR1.5 high dose plate exhibit a perfect linear behaviour with doses up to 300 cGy, where saturation occurs.

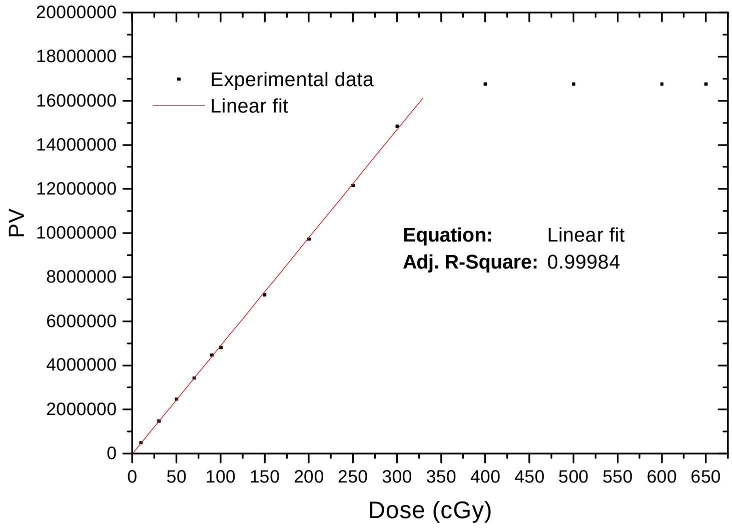

Figure 5.1: Calibration curve of the CR imaging plate obtained at a 6MV beam and 10 cm depth.

5.1.2 ENERGY DEPENDENCE

Energy dependence was verified by irradiating the plate in a solid water phantom at a 5 cm depth, to a dose of 100 cGy, in 6 MV and 18 MV beams. Pixel values registered for both energies are summarized in Table 5.1. Two observations can be made from these two measurements. First, the readout deviation between 6 MV and 18 MV is 27% (deviation calculated from the average reading). Secondly, the readout for 18 MV is lower than that at 6 MV. These combined results prove the strong energy dependence and the high sensitivity of the plate to low energy photons. Indeed, the 18MV beam is more penetrating and exhibits less scattering than does the 6 MV beam, which explains the higher reading at 6 MV.

Table 5.1: Energy dependence of the CR imaging plate at a dose of 100 cGy.

Energy	**Readout at 100 cGy**
6MV	4930
18MV	3750

5.1.3 FIELD SIZE DEPENDENCE

Field size dependence was performed by exposing the plate to a dose of 100 cGy at a depth of $z = 6cm$, for different field sizes in a solid water phantom measuring $30 * 30 cm^2$. Measurements were obtained with the use of high atomic number filters; 0.2 mm of tungsten and 0.8 mm of lead were placed on both sides of the plate with 1 cm of solid water between the plate and filters, as recommended by Olch[50]. The aim of the filters is to absorb low energy scattering photons that are more likely to interact with the plate, as proven in section 5.1.1. Inserting filters in both sides of the plate is dictated by the fact that low energy photons are scattered in all directions with the same probability. Pixel value dependence on field size is plotted in Fig 5.2. The figure shows that pixel value increases with field size; however, it decreases from the field size $30*30cm^2$ to $40*40cm^2$. This is attributable to the lack of scattering from the solid water since its size was exactly $30*30cm^2$. The deviation of pixel value between field sizes $5*5cm^2$ and $20*20cm^2$ is 19%, while the deviation on pixel value observed in the IP is approximately 15% between the fields $10*10cm^2$ and $30*30cm^2$. We can conclude that CR1.5 high dose displays strong field size dependence even with the presence of filters.

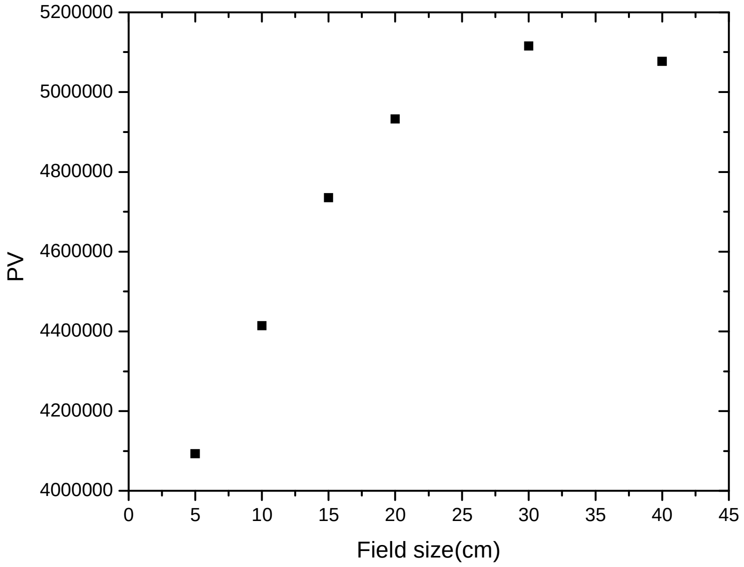

Figure 5.2: Pixel value of the CR imaging plate versus field size obtained at a 6MV beam and a dose of 100 cGy. Decrasing of PV from $30*30cm^2$ to $40*40cm^2$ is attributable to the lack of scattering from the solid water, which had dimensions of $30*30cm^2$.

5.1.4 ENHANCED DYNAMIC WEDGE

The measurements for the sixty degree enhanced dynamic wedge (EDW) were performed with the CR1.5 high dose. The CR plate was exposed in a solid water phantom, to 100 MU at 100 cm SSD, at two depths: $z_{\max} = 1.5cm$ and $z = 10cm$, with a field size of $10 * 20cm^2$. At each depth, one measurement was performed with the CR plate alone, and another measurement was obtained by using the CR and a filter that consisted of 0.2 mm of tungsten in the top of the plate. CR profiles were compared to that obtained with an array of ionization chambers; relative dose was considered as the relative pixel value without taking into account any correction for field size dependence. Figure 5.3 shows that, at a depth of $z_{\max} = 1.5cm$, measurements obtained with the CR alone agree with those from the ionization chambers, except in the region of high doses; however, the dose in the umbra region is definitively overestimated by the CR. Measurement with the filtered CR does not improve the response outside of the field; they agree everywhere with those obtained with the CR alone, except in the region of high dose where reproducibility of ionization chamber measurements is better with the CR alone. Figure 5.4 shows the profile of EDW at a depth of $z = 10cm$. Comparison between the profiles obtained with the array of ionization chambers and the imaging plate shows that reproducibility of the slope is better with the filtered CR; however, this is not the case when approaching the high dose region where the size of the field is definitively not accurate. Measurements with the CR alone reproduce the dimensions of the field, disagree with the slope obtained with the ionization chambers, and overestimate the dose in the umbra region. The deviation between the results obtained with non filtered CR and the ionization chambers reaches 6.7% at $z_{\max} = 1.5cm$, and 17% at $z = 10cm$. During irradiation with the enhanced dynamic wedge, the dose rate changes. If we assume that there is no dose rate dependence with the CR plate, then the higher

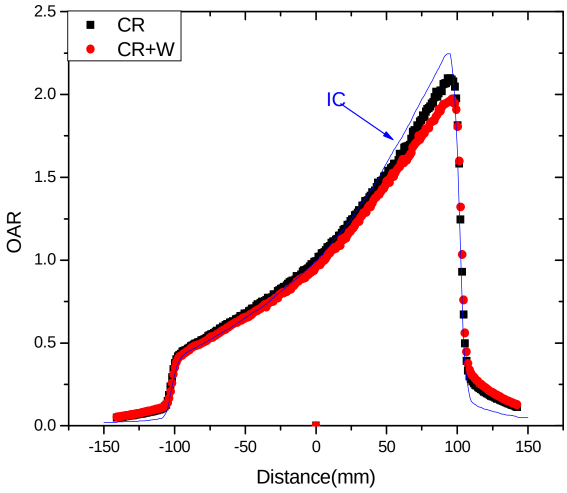

Figure 5.3: Comparison between the enhanced dynamic wedge measurements obtained with the CR1.5 (with and without tungsten, W) and that obtained with an array of ionization chambers. Measurements are performed at the depth of $z_{\max} = 1.5\,cm$.

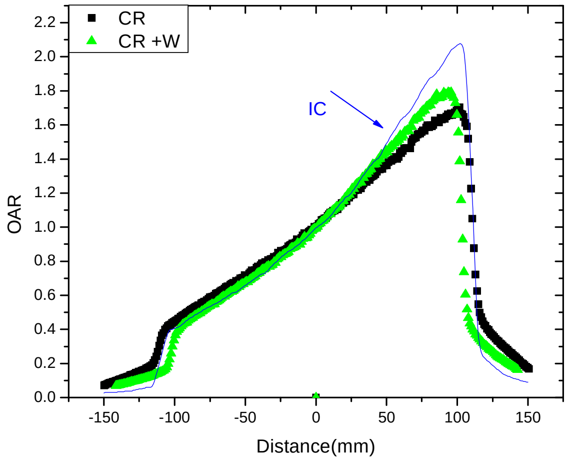

Figure 5.4: Comparison between the enhanced dynamic wedge measurements obtained with the CR1.5 (with and without tungsten, W) and that obtained with an array of ionization chambers. Measurements are performed at the depth of $z = 10\,cm$.

scattering at a depth of $z = 10\,cm$ may be the reason for the aforementioned higher deviation compared to that registered at $z_{\max} = 1.5\,cm$. Therefore, the applied filtration or the used protocol must be revised for the measurement of EDW.

5.1.5 CONCLUSION 1

In conclusion, this study shows the linearity of the CR, but the used protocol suggests strong energy dependence and field size dependence. The sixty degree enhanced dynamic wedge measurements registered with an array of ionization chambers are not perfectly reproducible with the CR, particularly at deeper depths and in the umbra region. The high atomic number filters, used to correct the energy dependence of the plate, did not improve results. Therefore, the use of the CR1.5 high dose with the Agfa ADC solo digitizer for dosimetry needs further investigation for an adequate protocol.

5.2 EBT FILM CHARACTERIZATION

5.2.1 FILM ABSORBANCE SENSITIVITY

An IMRT QA film was scanned, registered in RGB mode in a tagged image file format (TIFF), and then read on MATLAB. 250 cGy was the maximum dose received by this film; the composition of the three channels was extracted. The obtained images corresponding to the red, green and blue channels are presented in Fig 5.5, Fig 5.6 and Fig 5.7, respectively. Comparison of the three images illustrates a superior contrast with the red channel, which also corresponds to the highest absorbance of EBT films, as shown in Fig 3.3. Since 200 cGy is the most frequent dose fraction encountered in clinical context, the protocol used with EBT consists of extracting the red channel.

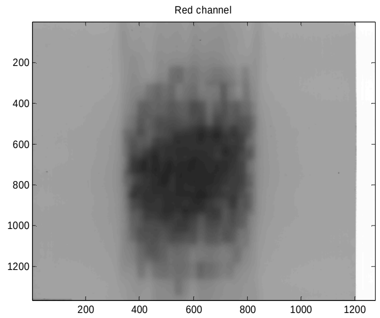

Figure 5.5: Image obtained after extraction of the red channel form the RGB image, maximum dose=250 cGy.

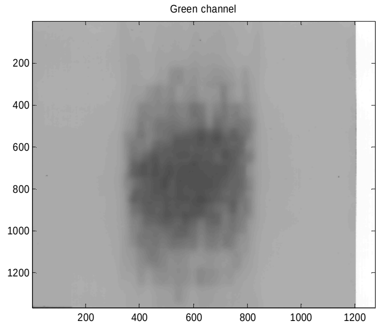

Figure 5.6: Image obtained after extraction of the green channel form the RGB image, maximum dose=250 cGy.

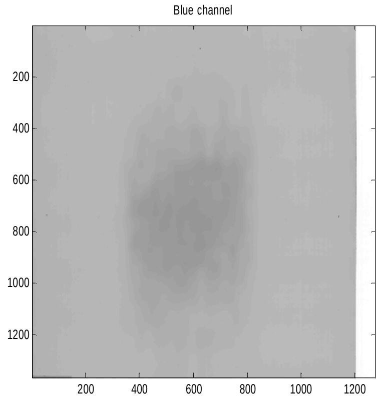

Figure 5.7: Image obtained after extraction of the blue channel form the RGB image, maximum dose=250 cGy.

5.2.2 SENSITIVITY OF EBT TO LIGHT

To verify the sensitivity of EBT to light, three pieces of EBT were used. The first piece was exposed to a fluorescent lamp; the second was exposed to an incandescent light, and the third was exposed to another incandescent light. Films were scanned prior to being exposed to light and after 15 minutes, 30 minutes and 1 hour of light exposure. The variation of pixel value due to light exposure and obtained with MATLAB, is plotted in Fig 5.8. The latter shows that the films systematically increase their coloration under a fluorescent light, while a deviation of 200 pixel values (PV) are observed in the case of the incandescent lamps. These 200 PV deviations were observed on different regions of an unexposed film, which means that this signal can also be attributable to a noise rather than a change of colour due to light exposure. This experiment shows that, in comparison to radiological films, EBT films are not sensitive to incandescent light (for less than 1 hour exposure), but must be kept far from fluorescent light.

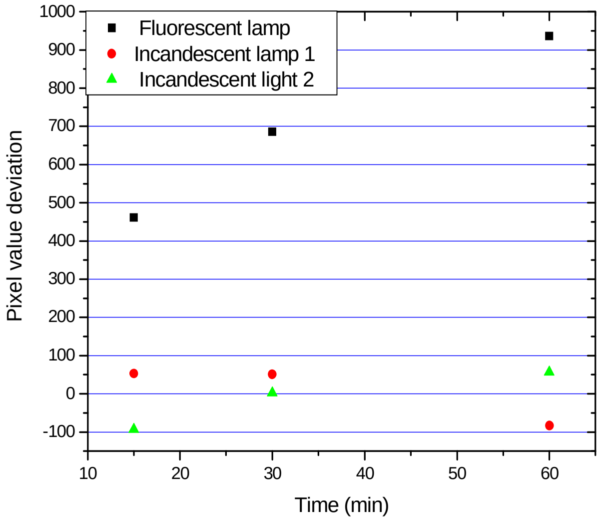

Figure 5.8: Absolute pixel value deviation on EBT films exposed to fluorescent and incandescent light.

5.2.3 EBT COLORATION WITH TIME

This section presents an investigation into the changes of coloration on EBT film with time, following exposure. For the purpose of this study, pieces of EBT film were exposed to known doses; each piece of film was scanned at different time intervals, and read with MATLAB. A calibration curve (dose versus pixel value) was obtained with the films that were scanned 24 hours after exposure. This calibration curve was used to convert PV to a dose value relative to the different times. The change of coloration was expressed as the percentage dose deviation compared to that obtained after 24 hours. Results are plotted in Fig 5.9 for each known dose. Figure 5.9 (logarithm scale in horizontal axis) shows a fast increase of dose with time, followed by a slower increase after 24 hours; this increase is more pronounced for lower doses. For example, the dose deviation after two days is 2.49% at 5 cGy, 1.81% at 10 cGy, and 1% at 350 cGy; whereas, after three weeks, it is equal to 13.45%, 4.8% and 3.8% at doses of 5 cGy, 10 cGy, and 350 cGy, respectively. The high deviation registered for lower doses, relatively to that of higher doses, suggests that this dose deviation can be attributable to the fluorescent scanner light, temperature, and humidity, instead of the irradiation itself. The highest change of coloration on one piece of film occurs in the first hours and then it stabilizes; for this reason, it is important that the delay time between the exposure and the scanning remains the same as the delay used to obtain the calibration curve. However, one should avoid the first hours where rapid color changes occur.

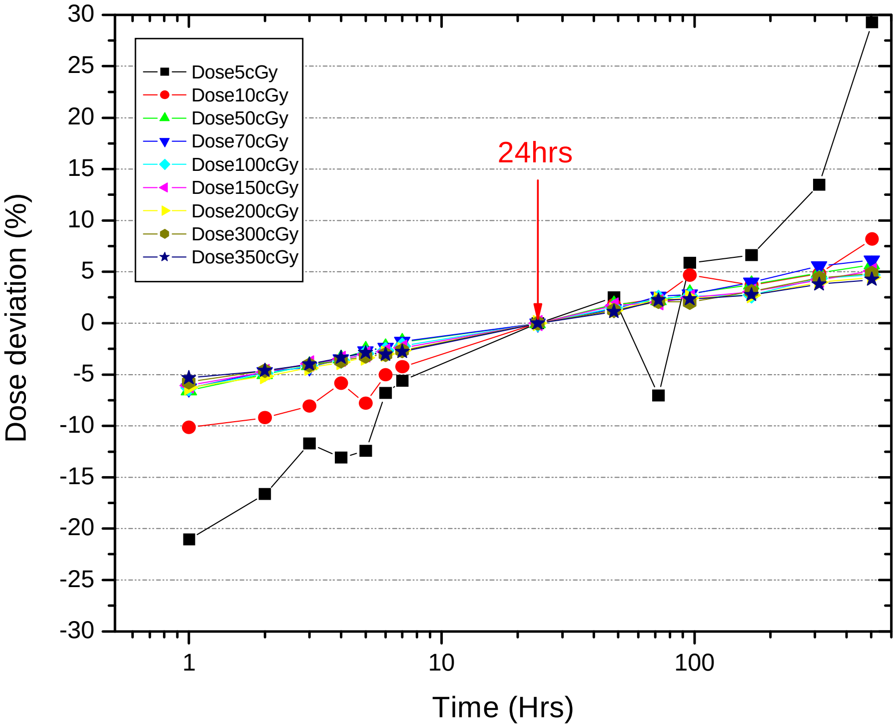

Figure 5.9: Change of EBT coloration with time, expressed in percentage dose deviation. The most significant variation of coloration is observed at 5 cGy; this is attributable to the effect of the fluorescent light scanner rather than irradiation.

5.2.4 EBT UNIFORMITY

To study EBT film uniformity, a film was cut into 50 small sections, and each one was labelled to keep track of its original position in the film. The 50 pieces were then irradiated at the same known dose. Four EBT films were used since four specific doses were chosen to evaluate EBT uniformity. From those four films, a total of 200 pieces were irradiated by exposing three pieces of film at a time, close to each other and near the central axis region. Irradiation was performed at a 5 cm depth in a solid water phantom. Previous profile measurements performed with ionization chamber showed that dose deviation from the central axis would not exceed 1.1%. Ionization chamber readings were taken at a 10 cm depth to track any changes on the linac's output. All pieces were scanned one by one, at the same position on the scanner bed, and read with MATLAB. As mentioned previously, each of the four films were related to a specific dose and divided into 50 pieces. Among the 50 pieces irradiated to the same dose, the one positioned at the center of the original film was chosen to acquire a calibration curve that was used to calculate the dose received by all the 200 pieces. The calculated deviation from the actual received dose, (ΔD), is given by $\left(\sqrt{(1.1/100)^2 + (dev)^2}\right)$ where (1.1%) and (dev) correspondingly represent the percentage dose deviation due to the beam profile, and the film non uniformity. Percentage dose deviation results due to the non homogeneity of EBT film, or (dev), are presented by histograms shown in Fig 5.10, Fig 5.11, Fig 5.12, and Fig 5.13, for the doses of 200 cGy, 100 cGy, 50 cGy, and 10 cGy, respectively. Table 5.2 summarizes the maximum dose deviation observed, the average dose deviation, and the number of films within one and two standard deviations. Table 5.2 shows that the maximum deviation, as well as the average deviation, decline as the dose increases. These results suggest a more consistent response from the film for higher doses, and a less uniform response at low doses. This fact can be attributable to a low signal to noise ratio observed at low doses, rather than an intrinsic non uniformity which affects the dose resolution.

Table 5.2: Summary of dose deviation due to film nonuniformity for different exposed doses.

Dose (cGy)	200	100	50	10
Maximum deviation (%)	2.3	4.3	4.73	10.24
Average deviation (%)	0.93	1.19	1.224	2.4
Standard deviation	0.63	0.92	1.13	2.6
Percentage of regions within one standard deviation	61	69	78	88
Percentage of regions within two standard deviation	98	96	92	90

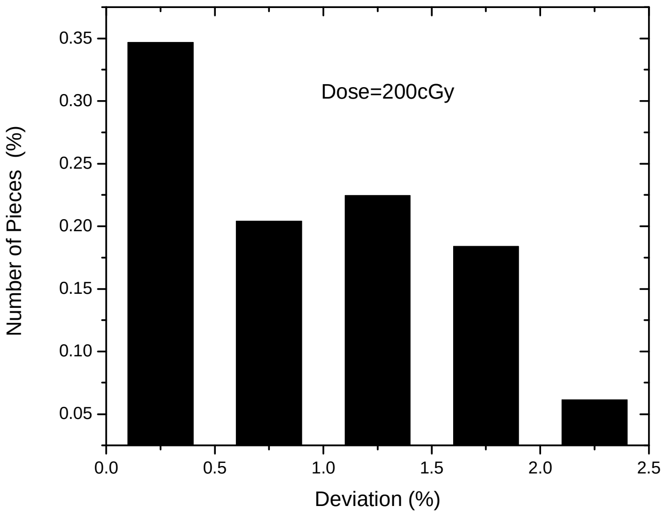

Figure 5.10: Histogram of dose deviation at 200 cGy due to film nonuniformity.

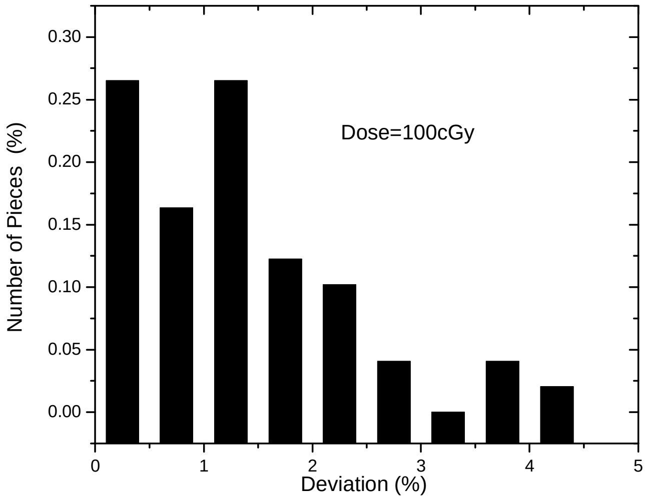

Figure 5.11: Histogram of dose deviation at 100 cGy due to film nonuniformity.

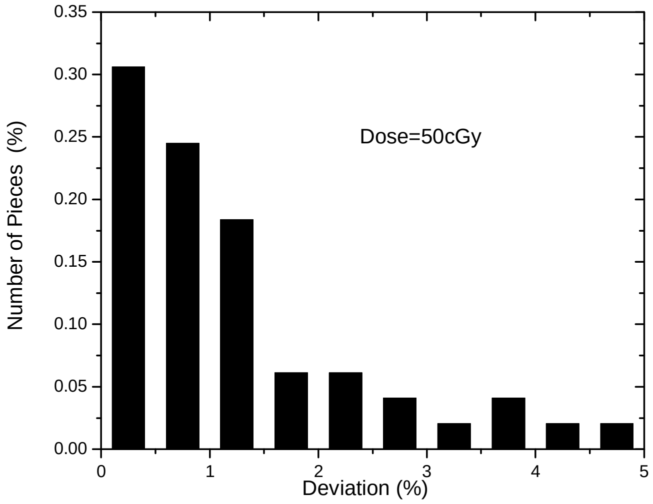

Figure 5.12: Histogram of dose deviation at 50 cGy due to film nonuniformity.

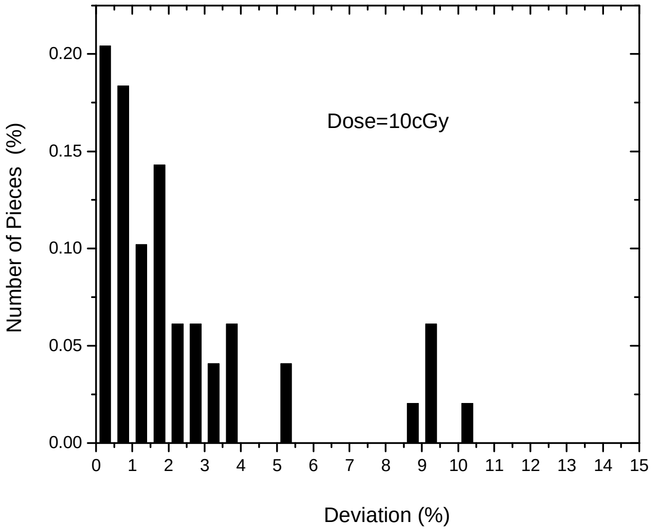

Figure 5.13: Histogram of dose deviation at 10 cGy due to film nonuniformity.

5.2.5 EBT ENERGY DEPENDENCE

Films were exposed to different doses at 6 MV and 18 MV beams, with a $10*10cm^2$ field size, and at a 5 cm depth. Films were scanned at the center of the scanner bed and read with MATLAB. Figure 5.14 shows the obtained calibration curves of EBT for both energies; they are similar. We can conclude that EBT is not energy dependant in the megavoltage range.

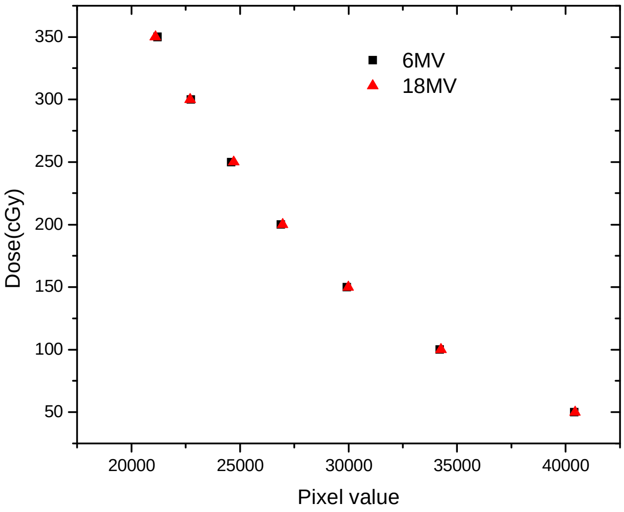

Figure 5.14: EBT calibration curves obtained at 6 MV and 18 MV.

5.2.6 EBT FIELD SIZE DEPENDENCE

Films were exposed to a dose of 100 cGy at a 5 cm depth with different field sizes. They were scanned in the center of the scanner bed and read with MATLAB. Figure 5.15 shows the percentage deviation of PV on EBT versus the field size. The field size reference was $10*10cm^2$. At a field size reaching up to $30*30cm^2$, maximum deviation on pixel value is 300 PV; though, a difference of 770 PV was observed during the study of EBT uniformity, in which case the average dose deviation was 1.19%. Therefore, we can conclude that EBT films are not sensitive to field size. Beyond a $30*30cm^2$ field size, the increase in pixel value, which indicates a decrease in dose, is attributed to a lack of scattering from the phantom, measuring precisely $30*30cm^2$.

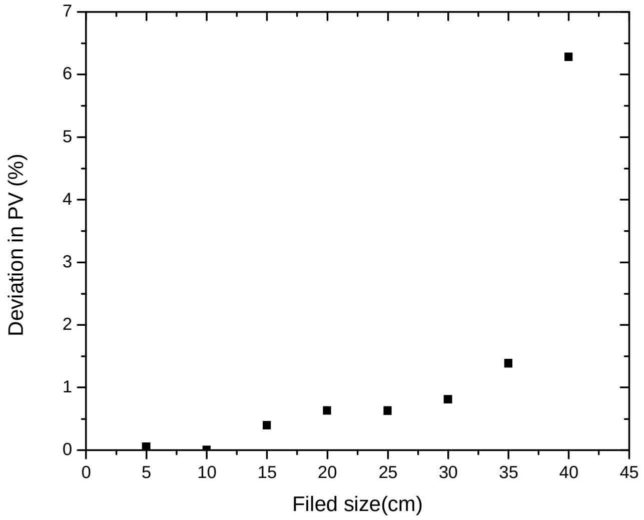

Figure 5.15: EBT pixel value variation versus field size at a dose of 100 cGy. (pixel value variation is calculated from that obtained at $10*10cm^2$).

5.2.7 EBT DEPTH DEPENDENCE

Pieces of EBT film were irradiated to a dose of 100 cGy at different depths, in a solid water phantom. Films were scanned in the center of the scanner bed, and read with MATLAB. Deviation of pixel values in percentage is plotted in Fig 5.16; 10 cm was the reference depth.

The maximum deviation of pixel value (from that registered at 10 cm) obtained over various depths is equal to 312 PV; it is less than the 700 PV deviation observed when studying EBT uniformity for the 100 cGy dose. We can then conclude that EBT is not sensitive to the depth of irradiation.

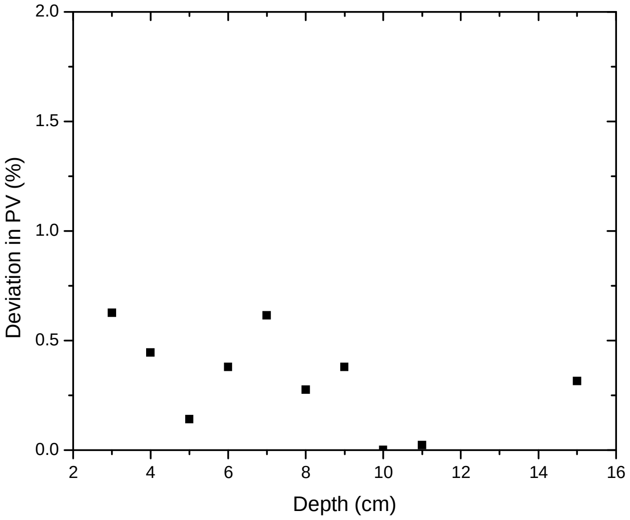

Figure 5.16: EBT pixel value variation versus depth at a dose of 100 cGy. (pixel value variation is calculated from that obtained at 10 cm).

5.2.8 EBT DOSE RATE DEPENDENCE

Pieces of EBT film were irradiated to a dose of 100 cGy at a 5 cm depth and a $20*20cm^2$ field size, in a solid water phantom. All the dose rates available on the linac were evaluated. Films were scanned in the center of the scanner bed, and read with MATLAB. Percentage deviations in PV are plotted in Fig 5.17; the reference dose rate was equal to the nominal 400 MU/min. The maximum pixel value deviation (from that obtained at the reference dose rate) was 495 PV. This result is less than the 700 levels observed when studying EBT uniformity for a dose of 100 cGy. We can then conclude that EBT is not sensitive to dose rate.

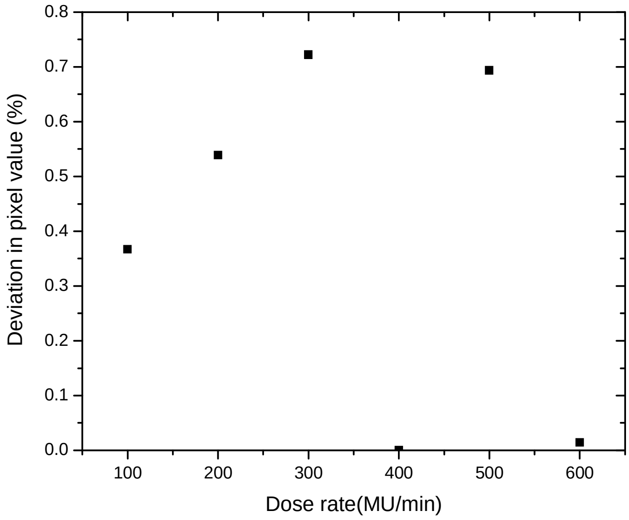

Figure 5.17: EBT pixel value variation versus dose rate at a dose of 100 cGy (pixel value variation is calculated from that obtained at 400 MU/min).

5.2.9 LANDSCAPE VERSUS PORTRAIT ORIENTATION

The manufacturer of EBT films recommends that the user scans the films in the landscape rather than in the portrait orientation. The first configuration means that the scanning direction, which corresponds to the CCD array motion, is parallel to the small size of the film; on the other hand, scanning in portrait orientation means that CCD move parallel to the large size of the film. This recommendation suggests a difference between the obtained pixel values in both orientations; this difference was measured and verified. A $1*2\ inch^2$ piece of film, exposed to a dose of 5 cGy, was scanned at different angles on the scanner bed while the centre of the film remained at the same position on the scanner bed. Images were registered and read on MATLAB. Figure 5.18 shows the variation of pixel value, versus different angles. In this plot, 0^0 ,180^0, and 360^0 angles correspond to the portrait orientation, while 90^0 and 270^0 angles stand for the landscape orientation.

Figure 5.18 illustrates a periodic pixel value. This result indicates that polymers of EBT films are sensitive to light polarization, and it emphasises the importance of maintaining the same orientation during scanning.

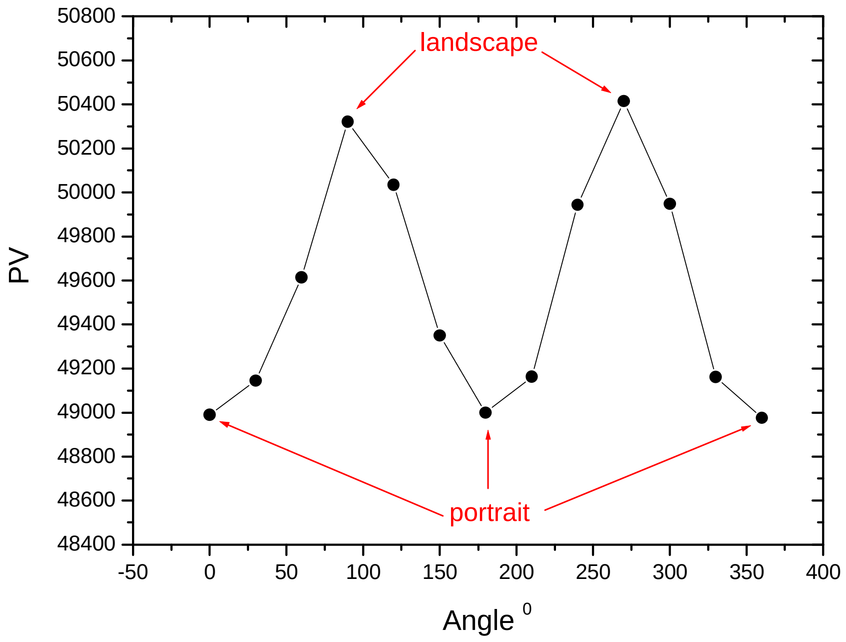

Figure 5.18: Orientation effect on EBT pixel value.

5.2.10 SCANNER CHARACTERIZATION WITH EBT

Scanner characterization is an important task to be performed by the physicist. Indeed, significant deviation of pixel values over the scanning surface have been previously observed. These are referred to as scanner artifacts, and they are attributed to light scattering effects[58]. The evaluation of these artifacts was performed with EBT by using the following method. Four pieces of film, exposed to doses of 50 cGy, 100 cGy, 200 cGy, and 300 cGy, were scanned in the portrait orientation; they were correspondingly positioned in different rows and columns, on the scanner bed. The images were read on MATLAB, and pixel values were normalized to those obtained in the center of the EPSON1680 scanner. Results obtained over the central row of the scanner bed are presented in Fig 5.19.

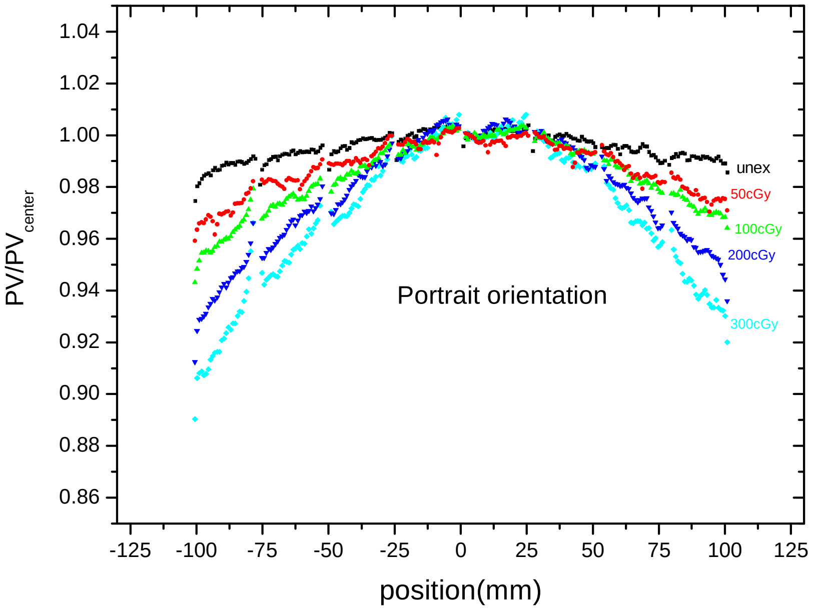

Figure 5.19: Normalized pixel value obtained at different doses when scanned at the central row of the scanner bed in the portrait orientation.

The behaviour of the scanner reading is the same for all doses; pixel values are lower at the edges of the scanner in contrast with those in the center of the scanner. Also, this effect is more pronounced for higher doses. For example, the lowest normalized pixel values are 0.9 for 300 cGy, 0.92 for 200 cGy, 0.95 for 100 cGy, and 0.96 for 50 cGy. Thus, doses at the edges will appear higher than in the center of the scanner if this effect is not taken into account. Comparison between the different rows does not show a strong dependence on the row position; for example, this is shown in Fig 5.20 for films exposed to 200 cGy. We can then conclude that pixel value depends on horizontal positioning on the scanner bed (parallel to the CCD array). The peaks appearing in Fig 5.19 and

Fig 5.20 are attributed to signals at the film's edges. Section 5.5 presents a more detailed study of scanner artifacts for dose assessment with EBT.

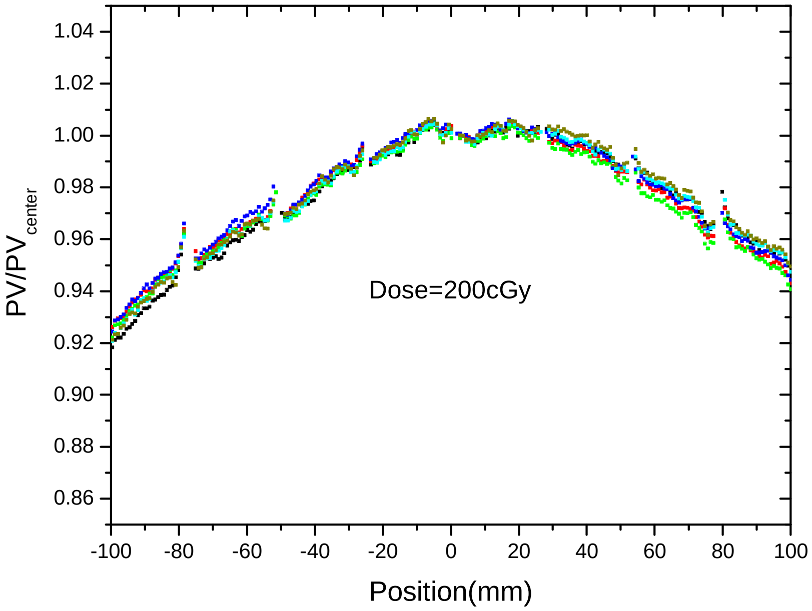

Figure 5.20: Normalized pixel value obtained at 200 cGy when films are scanned at different rows on the scanner bed in the portrait orientation.

5.3 EDR2 CHARACTERIZATION

5.3.1 EDR2 CALIBRATION CURVE

EDR2 films were cut as shown in Fig 4.7 and exposed as described in section 4.6; they were scanned at the center of the scanner bed. Figure 5.21 shows the variation of dose versus pixel value. The fact that pixel value at 10 cGy already corresponds to 35000 compared to 65536 $\left(2^{16}\right)$ shows the high sensitivity of EDR2.

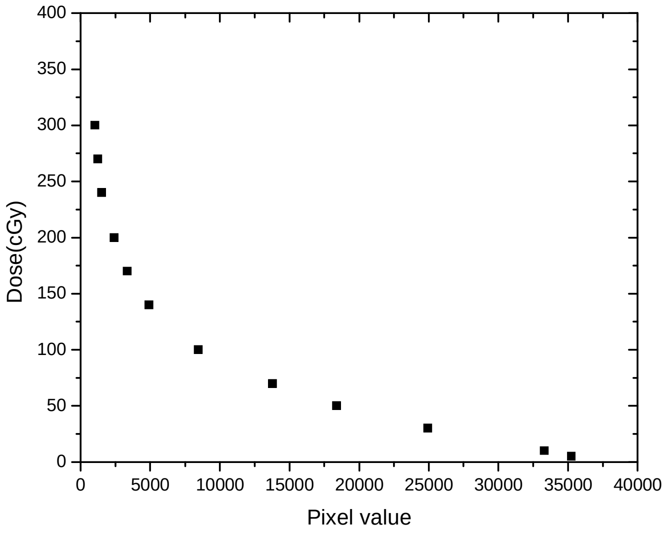

Figure 5.21: EDR2 calibration curve.

5.3.2 EDR2 REPRODUCIBILITY AND DEVELOPER ARTIFACTS

An unexposed EDR2 film was developed and scanned. The obtained image presented artifacts that were due to the quality of the developer; the arrows in Fig 5.22 point to some of these artifacts. Reproducibility was studied to evaluate the change of pixel value due to developer artifacts. For this purpose, 12 pieces of EDR2 film were cut and exposed to a dose of 100 cGy. Pixel values were converted to dose by using the calibration curve obtained in Fig 5.21. The average deviation from 100 cGy was 2.8%; four values exceeded 3% deviation; maximum deviation was 6.42%. This evaluation shows that developer artifacts affect the quality of the dosimetry system, and must be taken into account for the evaluation of an IMRT QA.

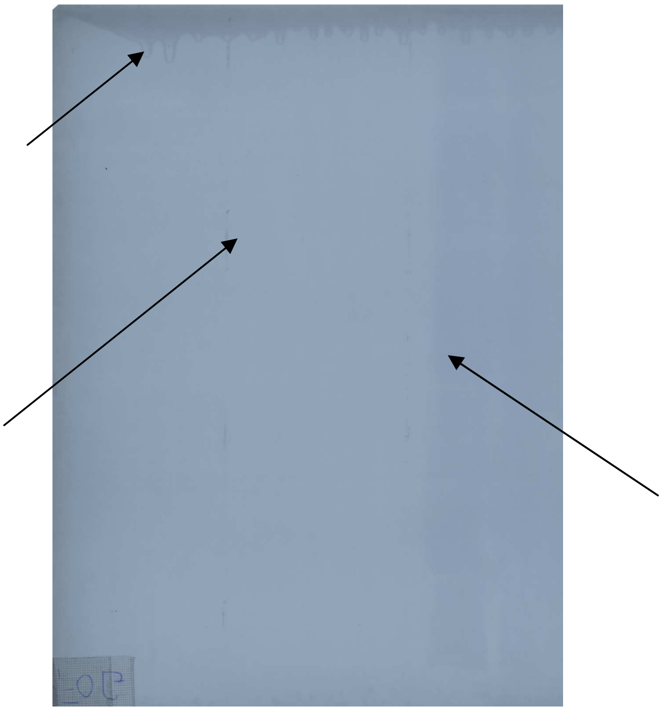

Figure 5.22: An unexposed EDR2 film; some developer artifacts are shown by the arrows.

5.3.3 EDR2 ENERGY DEPENDENCE

EDR2 energy dependence was investigated for two beam qualities on a 21VARIAN linac: 6 MV and 18 MV. EDR2 pieces, cut as shown in Fig 4.7, were exposed to different doses; they were scanned at the centre of the scanner bed, and read with MATLAB. Calibration curves for both energies are plotted in Fig 5.23; the curves are similar. We can conclude an energy independence of EDR2 in the megavoltage range.

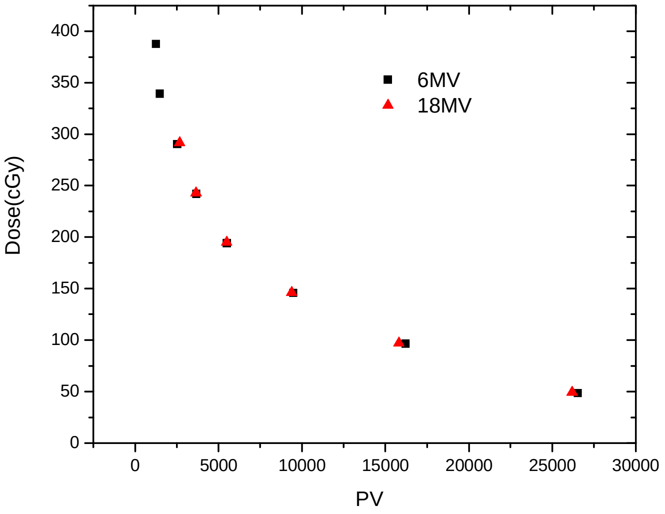

Figure 5.23: EDR2 calibration curves obtained at 6 MV and 18 MV.

5.3.4 EDR2 FIELD SIZE DEPENDENCE

Films were cut as shown in Fig 4.7. They were exposed to a dose of 100 cGy, at a 5 cm depth, at different field sizes in a solid water measuring $30*30cm^2$. The films were scanned in the center of the scanner bed, and read with MATLAB. Percentage pixel value deviations versus field size are plotted in Fig 5.24. Pixel values were converted to dose by using the calibration curve obtained in Fig 5.21; the deviation from 100 cGy was calculated. Results show a mean deviation of 3.1% with a standard deviation of 1.85%. The minimum deviation is 1.18% and the maximum deviation is 7.57%. In regards to the quality of the developer and to the processing conditions, which could be different from those when the calibration was performed, no conclusion can be made for EDR2 field size dependence.

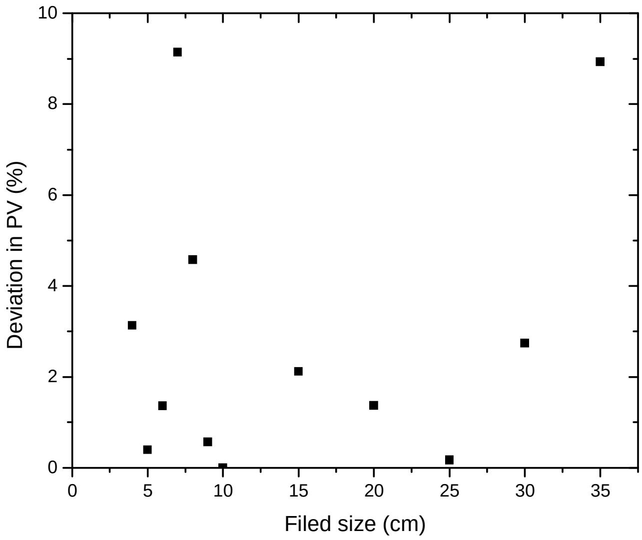

Figure 5.24: Percentage deviation of pixel value with EDR2 films versus field size.

5.3.5 SCANNER CHARACTERIZATION WITH EDR2 FILMS

A study of light scattering on EDR2 was performed to evaluate the impact of scanner artifacts on EDR2 pixel values. This was investigated by scanning the same piece of EDR2 at different positions on the scanner bed and read with MATLAB. When rotating one single film at the same position on the scanner bed, there was no observed difference between the portrait and the landscape orientation. Pixel values obtained at different regions of the scanner bed were normalized to that obtained in the center; results are plotted in Fig 5.25 for doses of 10 cGy, 50 cGy, 100 cGy, 200 cGy and 300 cGy. Figure 5.25 shows that normalized pixel values for doses of 10 cGy, 50 cGy and 100 cGy can be represented by one function, while another function is necessary for 200 cGy. Normalized pixel values for a 300 cGy dose, which is at the limit of the dynamic range, shows a big variation with the position on the scanner bed.

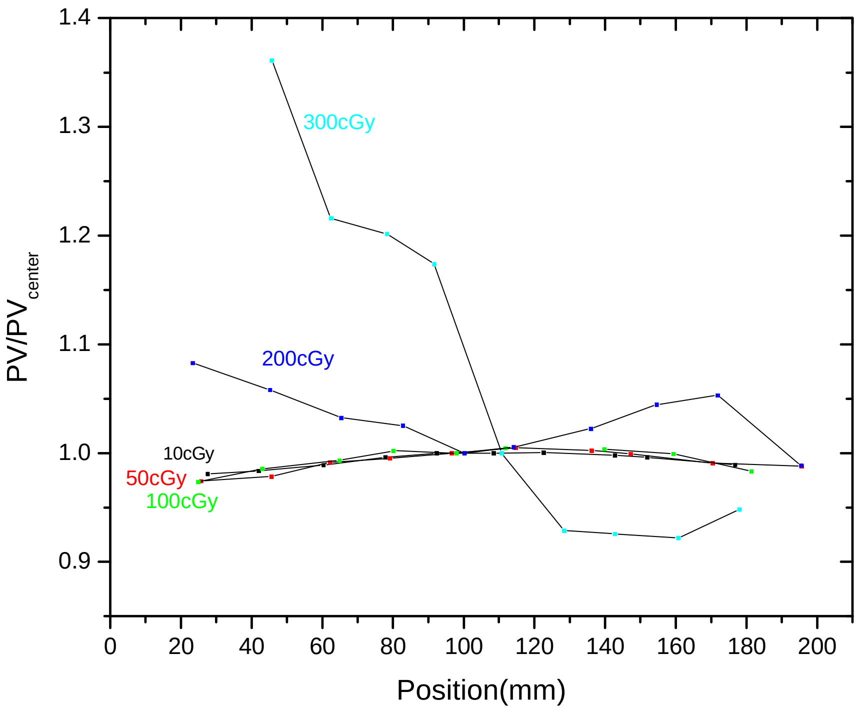

Figure 5.25: Normalized pixel values obtained with EDR2 at different column position on the scanner bed.

5.4 COMPARISON OF EBT VERSUS EDR2

5.4.1 COMPARISON OF CALIBRATION CURVES

Figure 5.26 shows the calibration curve obtained on EBT and EDR2 films. Comparison of both calibration curves shows that EDR2 is more sensitive than EBT (higher pixel value at low doses for EBT). However, radiological film saturates at 300 cGy. Therefore the dynamic range of the EDR2 film is lower than that of the EBT film, if the followed protocol consists of scanning EDR2 in the RGB mode, and extracting the red component. For doses less than 140 cGy, EDR2 has a higher variation of pixel values for a given variation of dose; this means that the contrast is better with EDR2. Compared to normalized pixel values obtained with EBT (see Fig 5.19), scanner artifacts versus dose are more important with EBT than with EDR2 for doses lower than 100 cGy; for example, the minimum normalized pixel value is 0.97 at the scanner's edges for doses less than 100 cGy, while it is equal to 0.95 for a dose of 100 cGy in the case of EBT. This fact, combined with the superior contrast of EDR2, suggests that scanner artifacts introduce higher error on dose assessment with EBT, compared to EDR2. However, developer artifacts are the main downside of EDR2.

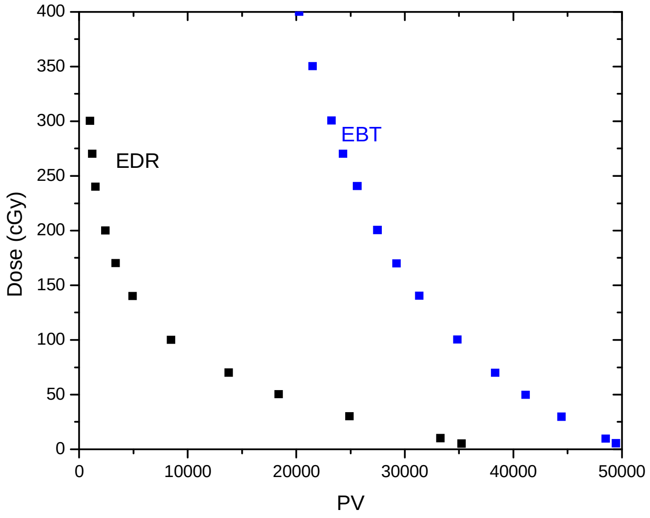

Figure 5.26: EBT and EDR2 calibration curve at 6 MV beam.

5.4.2 COMPARISON BETWEEN EDR2 AND EBT FOR IMRT QA

To evaluate EBT and EDR2 for IMRT QA, 13 clinical cases were chosen. Plans were calculated with the CORVUS treatment planning system (NOMOS Corporation, 200 West Kensinger Drive, Cranberry Township, PA 16066). One EBT and one EDR2 film were exposed together for the same QA plan, with the setup shown in Fig 4.3. Dynamic IMRT was performed on a Varian linac at a 6 MV beam; time delivery depends on the plan and can be up to 30 minutes. Both films were scanned 24 hrs after irradiation. This time frame was chosen for the EBT scan when its calibration was performed. Films were processed with the software FILMQA in the relative dose mode; isodoses were normalized to the isocenter. Table 5.3 summarizes the quantitative results obtained with the γ index; the simulated dose at the isocenter is presented in column 2, and the percentage of pixels that pass the criteria of (3%, 3mm) appears in columns 3 and 4 for EDR2 and EBT, respectively. These results indicate that ten cases out of the total thirteen show a superior percentage of pixels passing the criteria of the γ index with EDR2; one shows equivalent results while two are definitively better with EBT. Case number 9 is better with EBT; this is attributable to a strong presence of developer artifacts, as indicated by the arrows in Fig 5.27. Figure 5.28 shows the comparison of calculated and measured isodoses obtained with EDR2 for case 9; those obtained with EBT as compared to the plan, are illustrated in Fig 5.29. Figure 5.28 shows higher discrepancies on the 30%, 50%, and 70% isodose lines that are attributed to developer artifacts. Case 12 is definitely better with EBT because dose normalization in the center is 345 cGy; this is higher than the dynamic range of EDR2, where saturation of the scanner response leads to artifacts as shown in Fig 5.25. Isodoses for case 12, obtained with EDR2 and EBT as compared to the plan, are shown in Fig 5.30 and Fig 5.31, respectively.

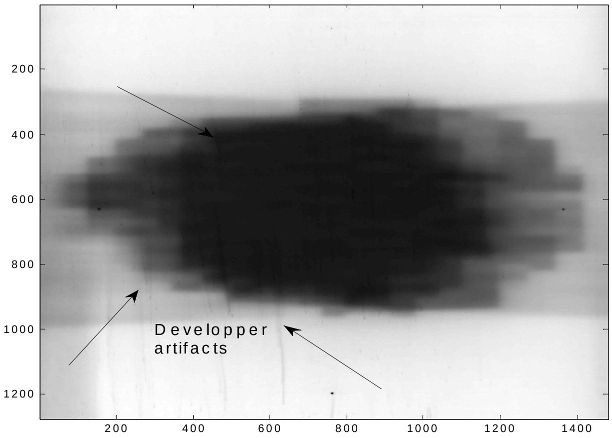

Figure 5.27: Scanned EDR2 film for the case 9. Some of developer artifacts are shown by the arrows.

Table 5.3: Percentage of pixels passing the criteria (3%, 3 mm) for the γ index. Results are obtained with EDR2 and EBT films.

Case	Dose (cGy)	EDR2	EBT
1	229	96.72	72.39
2	238	90.7	63.99
3	183	58.62	45.7
4	258	98.04	79.84
5	168	99.51	83
6	268	99.88	87.23
7	179	85.39	84.68
8	196	98.2	78.31
9	180	69.9	81.04
10	178	89.07	55.07
11	182	80.77	81.65
12	345	83.58	99.02
13	197	99.64	97.03

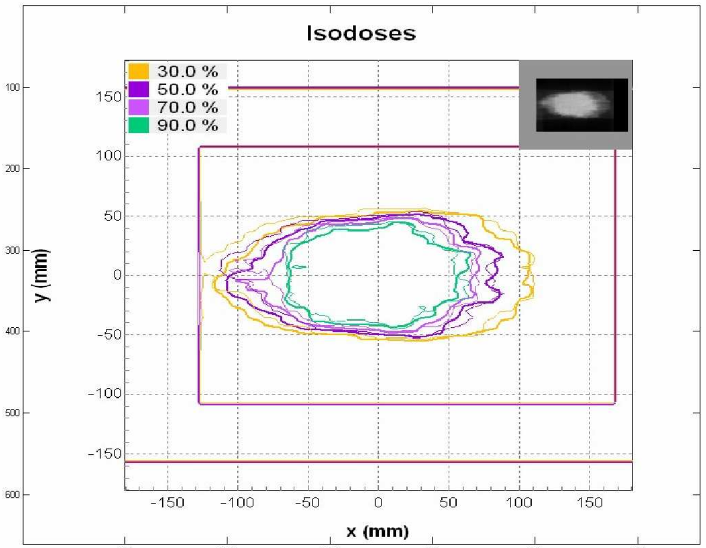

Figure 5.28: Isodoses for the case 9, obtained with EDr2 as compared to the plan (thicker lines represent the plan). Discrepancies among the 30%, 50% and 70% isodoses on the left region are attributed to developer artifacts.

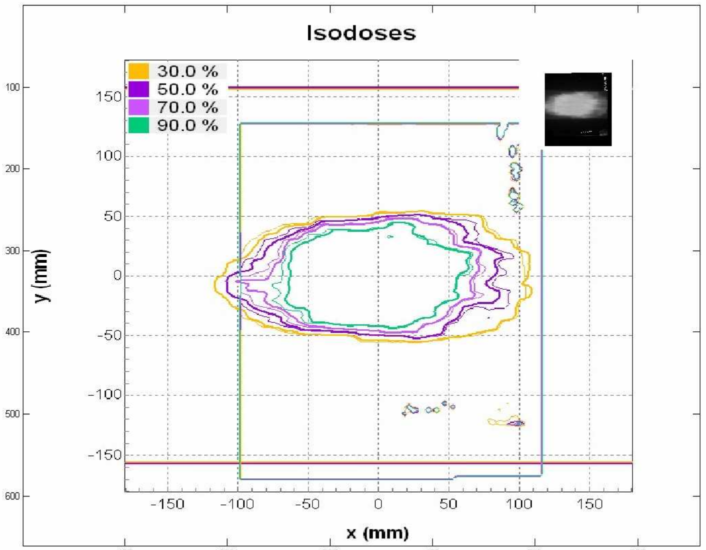

Figure 5.29: Isodoses for the case 9 obtained with EBT as compared to the plan (thicker lines represent the plan); better coincidence on the isodoses is obtained compared to that obtained wit EDR2 (as shown in Fig 5.28).

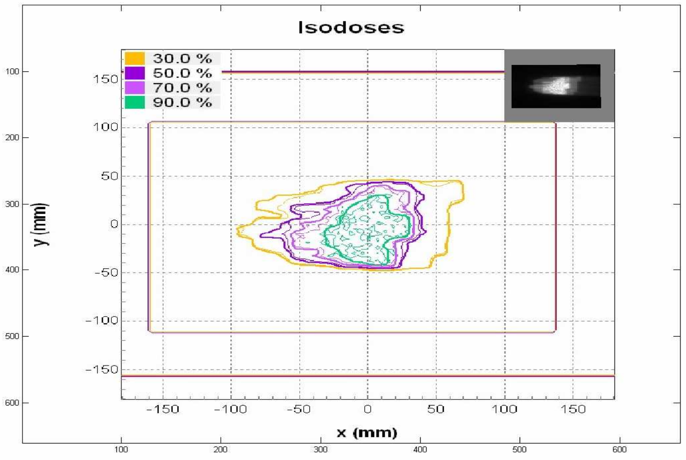

Figure 5.30: Isodoses for case 12 obtained with EDR2 as compared to the plan (thicker lines represent the plan); the measured 90% isodose (310 cGy) does not reproduce the calculated one; this is attributable to scanner artifacts observed at this dose level as shown in Fig 5.25.

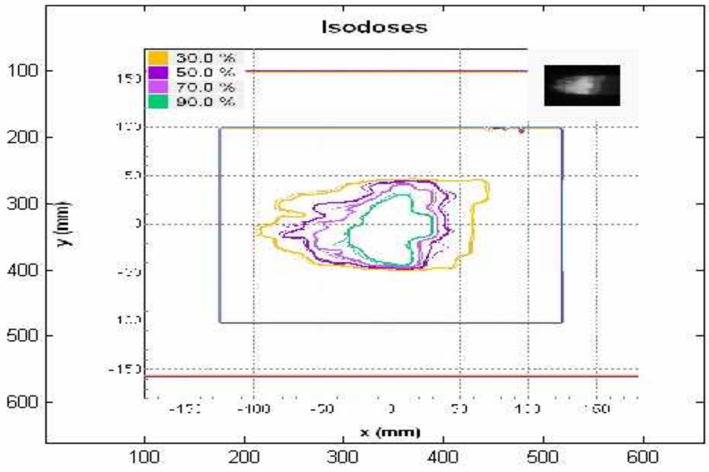

Figure 5.31: Isodoses for case 12, obtained with EBT as compared to the plan (thicker lines represent the plan); better coincidence on the isodoses is obtained compared to that obtained with EDR2 as shown in Fig 5.30.

5.4.3 CONCLUSION 2

The superior contrast on EDR2, in comparison with EBT, makes scanner artifacts less important with EDR2 . This can explain why better results are obtained with the γ index in the relative dose mode. However, there are downsides to using EDR2 for dosimetry. The need of the developer must involve careful quality assurance regarding the cleanliness of the different baths; in addition, the limited dynamic range of EDR2 (if scanned in the RGB mode) leads to better results with EBT. The higher atomic number of EDR2 material $(Z = 43)$compared to that of EBT material $(Z \approx 7)$ makes radiological films more sensitive to low energy photons; this is a good reason not to use EDR2 in absolute dosimetry.

5.5 IMPACT OF SCANNER ARTIFACTS ON EBT FILMS

A study was performed to investigate the impact of scanner artifacts on dose assessment when using EBT films and the EPSON1680 scanner. As shown in Fig 5.20, scanner artifacts strongly depend in which column the film is placed on the scanner bed; however, dependence on the row position is weak. This means that a calibration curve is needed at every column position on the scanner bed for an accurate dose assessment. Therefore the simplest way of doing this is to scan every film exposed to a known dose at different columns in the digitizer and acquire a calibration curve relative to a particular column position on the scanner bed. The consecutive scans relative to known dose were performed at 0.5 inch increments, at the central row of the scanner bed; four EBT films (instead of one) were used in order to avoid additional color change due to the fluorescent light of the digitizer. Of course, this procedure is perfectly valid if the uniformity of EBT is ideal, yet as shown in Table 5.2, the worst measured average non uniformity is 2.4%, obtained at 10 cGy. The images obtained from the central column position of the scanner were used to acquire a calibration curve with the software FILMQA, and a calibration curve with MATLAB. This first calibration curve obtained with MATLAB does not take into account scanner artifacts; we will refer to it as MATLAB (no correction). A Wiener filter was applied to all images processed in MATLAB in order to decrease the image noise due to imperfections in the films[39]. An additional protocol performed on MATLAB was introduced to correct for scanner artifacts. This procedure consists of recalculating a new calibration curve at each column position; we will refer it to as MATLAB (with correction). The procedure was done by following these steps:

1- For a known dose, pixel values versus position were plotted and fitted with a polynomial function of the 6^{th} degree, as shown, for example, in Fig 5.32 for the dose 550 cGy.

2- Each 6^{th} degree polynomial fit obtained in step 1 and related to a known dose, was used to calculate the pixel value that corresponded to the mentioned dose at different columns.

3- For each column, the dose was plotted as a function of the respective pixel value obtained in step 2. The curve was fitted with a polynomial function of the 6^{th} degree. Thus, a calibration curve was acquired at each column.

4- The calibration curve that corresponded to the known column was used to convert the pixel value of an image to a dose.

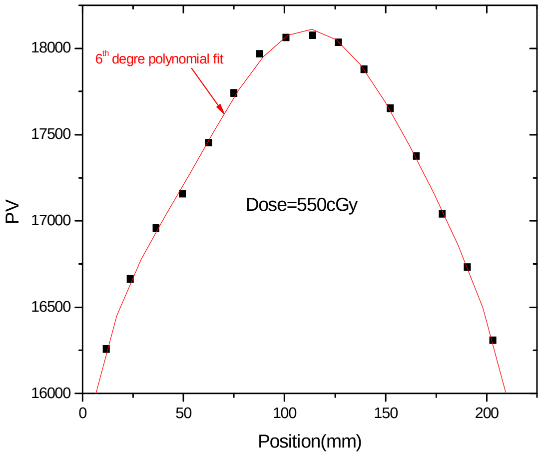

Figure 5.32: Pixel value of EBT versus its column position on the scanner bed for a dose equal to 550 cGy.

5.5.1 PROFILE MEASUREMENT WITH EBT

The effect of scanner artifacts was studied, first, by measuring profiles of an open field with EBT films. Six bands, each measuring $1*8\,inch^2$, were positioned at a 10 cm depth, in a solid water phantom measuring $30*30cm^2$. Irradiation was performed with an SSD setup at 10 cGy, 50 cGy, 100 cGy, 200 cGy, 300 cGy and 500 cGy in a $30*30cm^2$ field size. For every exposure, an ionization chamber measurement was performed to correct for any changes from the linac's output. Films were scanned and processed with FILMQA, with MATLAB (no correction), and with MATLAB (with correction). Results were compared to the profiles measured with an array of ionization chambers; they are plotted in

Fig 5.33. First, we can notice that results obtained with MATLAB (with correction) agree well with ionization chamber measurements. However, a discrepancy with the ionization chambers appears at 50 cGy; yet the highest disagreement is approximately 5%. The profile obtained at the 10 cGy dose (the scale at 10 cGy is different from the other five curves) shows high fluctuations

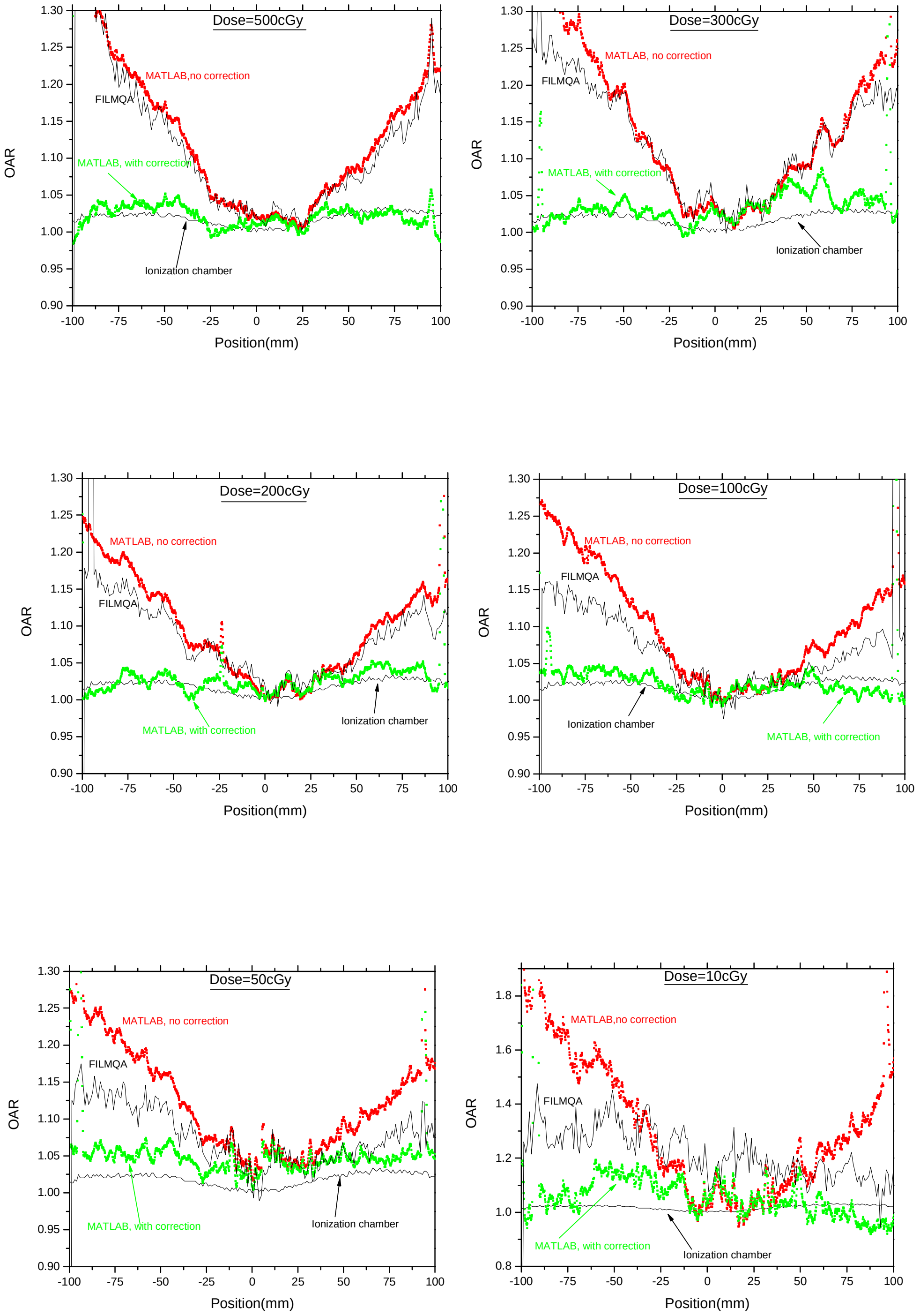

Figure 5.33: Measured profiles obtained with FILMQA, MATLAB (with and without correction) and the array of ionization chambers.

that are attributable to a low signal to noise ratio. Curves obtained with MATLAB (no correction) show the poorest results, an outcome when scanner artifacts are not taken into account. FILMQA results do not agree with ionization chamber profiles, hence we suspect that FILMQA does not correct for scanner artifacts; however, it should be noticed that results from FILMQA are better than those from MATLAB (no correction), particularly by decreasing dose. ΔD_M equals to 3% and 5% are the criteria applied for the dose difference that were used in this work. Hence, we compared the profile's results obtained by FILMQA with that obtained from the array of ionization chambers to identify the reliable region of the scanner bed (in millimetres) where these two criteria are achievable with FILMQA. Results are summarized in Table 5.4.

Table 5.4: Dimensions of the region on the scanner bed, relative to different doses, where the dose difference criteria of 3% and 5% are achievable.

	50 cGy	100 cGy	200 cGy	300 cGy	500 cGy
$\Delta D_M = 3\%$	73 mm	100 mm	56 mm	42 mm	61 mm
$\Delta D_M = 5\%$	109 mm	116 mm	106 mm	54 mm	87 mm

The study of scanner non-uniformities performed on MATLAB, as shown in Fig 5.19, indicates that the reliable region of the scanner bed should decrease when the dose increases; this fact is not observed when films are processed with FILMQA. Indeed, Table 5.4 shows that a region of 73 mm on the scanner bed is reliable at 50 cGy for $\Delta D_M = 3\%$. This dimension increases to 100 mm at 100 cGy, and decreases again for 200 cGy and 300 cGy; then, it suddenly increases at 500 cGy. The same behaviour is observed for $\Delta D_M = 5\%$. The profile corresponding to 10 cGy , shows that the minimum agreement between FILMQA and the ionization chamber measurements is 4%; the highest disagreement is approximately 15%. This result is attributable to the high noise detected at low doses, as was already observed in section 5.2.4. This fact affects low doses on the films as well as regions of high dose gradient. When a film is scanned, the actual signal that results from light transmission through the film is the deconvolution of the obtained signal with the response of the scanner; this is what FILMQA is supposed to do via the background correction. In the proposed protocol performed with MATLAB, the only correction applied to raw data is the Wiener filter; the latter aimed to decrease the image noise due to imperfections in EBT films, as Devic[39] has proposed. This correction gives acceptable results on the profiles, except at low doses. The next step consists of verifying the protocols used on IMRT QA plans.

5.5.2 IMRT QA WITH EBT

After verifying the correction done with MATLAB on simple cases such as profiles, the same method was performed on 15 IMRT QAs that were chosen from clinical cases. Plans were calculated with the CORVUS treatment planning system (NOMOS Corporation, 200 West Kensinger Drive, Cranberry Township, PA 16066). The first step consisted of comparing the results obtained with MATLAB, with and without correction, over the same region of interest. Images were converted to dose by the two methods: MATLAB (no correction) and MATLAB (with correction). Doses were corrected by taking into account the output of the linac since the treatment planning system calculates the dose based on an output of 100 cGy/100MU at maximum depth dose. Doses were normalized to the isocenter; isodoses were obtained, and the γ index was calculated. The chosen criteria were (3%, 3 mm) and (5%, 3 mm). Table 5.5 summarizes the results obtained with MATLAB (no correction) and MATLAB (with correction). Columns 2 and 3 present the number of pixels passing the criteria (3%, 3 mm) with MATLAB (with correction) and MATLAB (no correction), respectively. Columns 4 and 5 present the number of pixels passing the criteria (5%, 3 mm) with MATLAB (with correction) and MATLAB (no correction), respectively. The comparison of results obtained on MATLAB, with and without correction, shows that correcting for scanner artifacts leads to a significant improvement on the number of pixels passing a chosen criterion. This can also be concluded by comparing the isodoses of case 9880 depicted in Fig 5.34 and Fig 5.35, and the isodoses of case 9487 shown in Fig 5.36 and Fig 5.37; the displayed isodoses are equal to 30%, 50%, 70% and 90%.

Table 5.5: Percentage of pixels passing the criteria of the γ index at (3%, 3 mm) and (5%, 3 mm).

	MATLAB, with correction (3%, 3 mm)	**MATLAB, no correction (3%, 3 mm)**	**MATLAB, with correction (5%, 3 mm)**	**MATLAB, no correction (5%, 3 mm)**
Case 9181	84	51	88	57
Case 9649	59	26	69	33
Case 9569	63	58	73	68
Case 9487	38	24	47	31
Case 9766	74	43	82	49
Case 9449	77	58	85	65
Case 9484	72	44	81	51
Case 9879	79	52	85	58
Case 9128	58	34	68	42
Case 9886	87	60	94	69
Case 9883	76	47	83	55
Case 9880	91	57	96	63
Case 9230	84	59	90	65
Case 9231	68	47	81	56
Case 9046	80	57	89	66

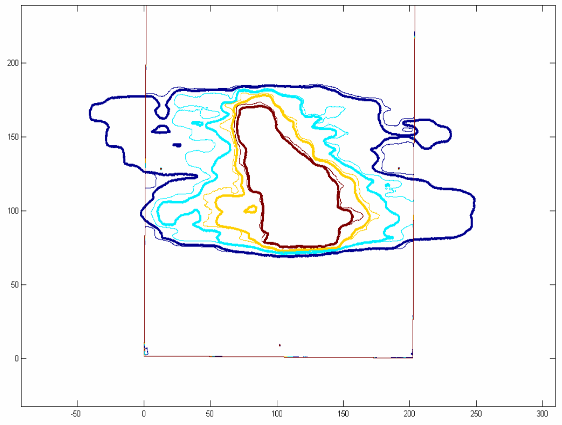

Figure 5.34: Isodoses of the case 9880, obtained by MATLAB (no correction). The dose at the center equals 212 cGy, thicker lines represent the plan. Displayed isodoses are 30%, 50%, 70% and 90%.

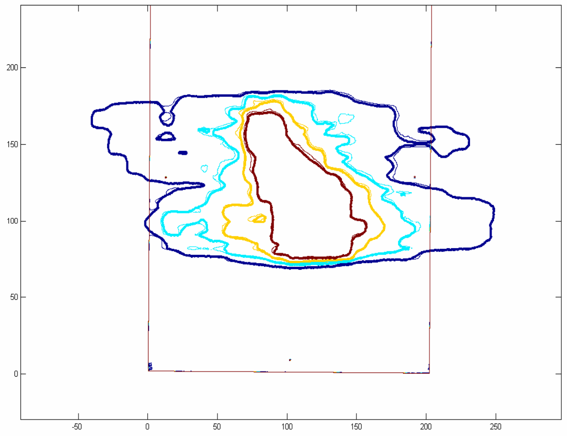

Figure 5.35: Isodoses of the case 9880, obtained by MATLAB (with correction); the dose at the center equals 212 cGy, thicker lines represent the plan. Displayed isodoses are 30%, 50%, 70% and 90%. Better agreement between the measured and calculated isodoses is obtained by correcting for scanner artifacts (As shown in Fig 5.34).

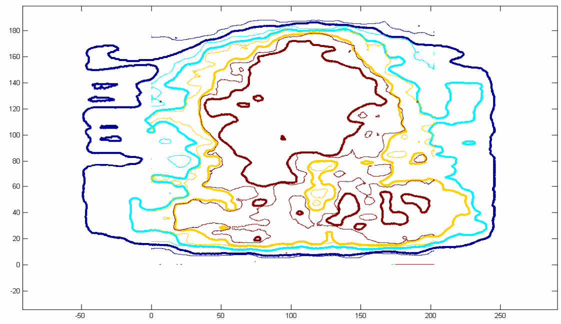

Figure 5.36: Isodoses of the case 9487, obtained by MATLAB (no correction); the dose at the center equals 177 cGy, thicker lines represent the plan. Displayed isodoses are 30%, 50%, 70% and 90%.

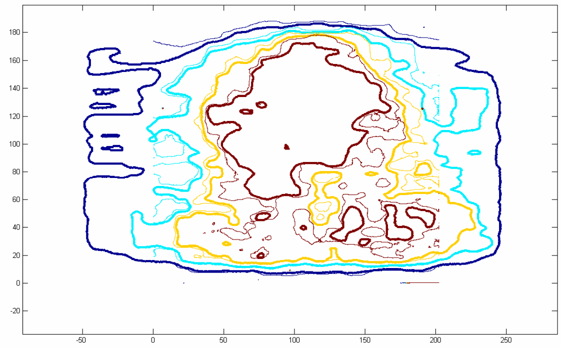

Figure 5.37: Isodoses of case 9487, obtained by MATLAB (with correction); the dose at the center equals 177 cGy, thicker lines represent the plan. Displayed isodoses are 30%, 50%, 70% and 90%. Better agreement between calculated and measured isodoses is obtained after correcting for scanner artifacts (as shown in Fig 5.36).

In the second step, a comparison was performed between the results obtained by MATLAB (with correction) and the FILMQA software, over the same region of interest. The quantitative evaluation is summarized in the Table 5.6 with the corresponding simulated dose. The latter is added because scanner artifacts are larger for higher doses (as shown in Fig 5.19). Columns FILMQA3 and FILMQA5 present the number of pixels passing the criteria (3%, 3 mm) and (5%, 3 mm), respectively, and obtained with the FILMQA software. Columns MATLAB3 and MATLAB5 present the number of pixels passing the criteria (3%, 3 mm) and (5%, 3 mm), respectively, and obtained with MATLAB. F3 and M3 present the mean of the γ index obtained with FILMQA and MATLAB for the criteria (3%, 3mm), while F5 and M5 present the mean of the γ index obtained for the criteria (5%, 3 mm). Comparisons among the number of pixels passing the criteria (3%, 3 mm) show that 9 cases out of 15 are improved by MATLAB (with correction); however, only 2 cases out of 15 show an improvement in the average of the γ index. These two cases are case 9880 and case 9046; they correspond to the doses 212 cGy and 529 cGy at the isocenter. Since scanner artifacts increase with dose, these two improvements can be explained by the correction introduced on MATLAB; however, this does not explain why case 9231, which was irradiated to 351 cGy at the isocenter, is not improved. With regards to criteria (5%, 3 mm), case 9046 is the sole case that is drastically improved by MATLAB (with correction). Poor results are obtained for case 9569, case 9487, and case 9128; these had an isocenter dose of approximately 170 cGy while cases with the same dose are improved with MATLAB. This shows that the Wiener filter is probably not the only correction one should apply when processing raw data of the EPSON1680.

Table 5.6: Comparison between FILMQA and MATLAB (with correction) regarding percentage of pixels passing the criteria (3%, 3 mm), (5%, 3 mm) and the mean of the γ index.

	FILMQA3	**F3**	**MATLAB3**	**M3**	**FILMQA5**	**F5**	**MATLAB5**	**M5**	**Simulated dose (cGy)**
case 9181	81	0.64	84	0.95	92	0.5	88	0.66	160
case 9649	54	0.99	59	2.54	68	0.78	69	1.66	182
case 9569	89	0.56	63	1.08	97	0.43	73	0.79	167
case 9487	60	0.94	38	1.88	73	0.75	47	1.27	177
case 9766	62	0.86	74	0.99	81	0.66	82	0.73	163
case 9449	71	0.78	77	1.02	81	0.61	85	0.72	168
case 9484	76	0.68	72	0.94	86	0.54	81	0.69	161
case 9879	70	0.79	79	1.23	82	0.61	85	0.84	186
case 9128	77	0.68	58	1.56	92	0.53	68	1.09	167
case 9886	85	0.58	87	0.6	95	0.46	94	0.46	192
case 9883	69	0.77	76	1.12	82	0.6	83	0.81	182
case 9880	90	0.6	91	0.5	99	0.48	96	0.39	212
case 9230	92	0.5	84	0.7	99	0.39	90	0.53	201
case 9231	92	0.56	68	0.96	99	0.43	81	0.73	351
case 9046	57	0.89	80	0.72	75	0.69	89	0.55	529

5.5.3 CONCLUSION 3

Profiles of open beams, measured and processed on FILMQA, show a large discrepancy with that obtained with an array of ionization chambers; this discrepancy can be attributable to scanner artifacts, though a good agreement is obtained on MATLAB by taking them into account. This study shows that scanner artifacts strongly affect dose assessment with films, as shown on MATLAB with and without correction. When compared to the FILMQA software, the number of pixels passing the criteria (3%, 3 mm) for the γ index is improved on MATLAB (with correction) in nine out of fifteen cases; on the other hand, one out of fifteen cases is drastically improved for the criteria (5%, 3 mm) - a case where the dose range is up to 530 cGy. FILMQA gives inaccurate results on profiles, but it gives acceptable results for the number of pixels passing chosen criteria for the γ index. In conclusion, this study indicates the importance of choosing a protocol in dosimetry. Characterization of the signal to noise ratio of the CCD array, and its effect on dose assessment (for low as well as high doses), is an important feature for the use of flat bed scanners. It will certainly improve the protocol used in MATLAB (with correction).

Chapter 6: CONCLUSION

6.1 THESIS SUMMARY

In the first part of this thesis, a photostimulable phosphor system (referred to as computed radiography or CR) was evaluated for dosimetric purposes. The equipment consisted of an AGFA CR1.5 high dose, a product commercialized by AGFA (Agfa Corporation, 275 North street, Teterboro, NJ, USA) dedicated to be used as a portal imaging device; the digitizer was the AGFA ADC solo. Raw data were extracted from the digitizer, following the procedure of the manufacturer, and then processed in MATLAB by applying a Wiener filter. The proposed protocol shows the linearity of the CR, energy dependence, as well as a field size dependence that could not be corrected for by adding high atomic number filters. We conclude that further investigation is needed to find the best protocol for the use of CR in dosimetry.

The second part of this thesis consisted of comparing two widely used films in IMRT QA, namely, the radiological extended dose rate (EDR2) commercialized by KODAK (Eastman Kodak Company, Rochester, NY), and the radiochromic external beam therapy (EBT) commercialized by International Speciality Products (International Specialty Products, 1361 Alps road, Wayne, NJ, USA). The characterization of EBT films shows that it is sensitive to fluorescent light; its change of colouration due to irradiation is fast at the first hours. The time delay between the irradiation and the scan must remain the same as when the calibration was performed. The direction of the scan must always be the same because polymers of EBT are sensitive to the polarization of light. Comparison of calibration curves of both films shows that EDR2 is more sensitive than EBT; EDR2 has a better contrast, yet a lower dynamic range when scanned in the RGB mode. An investigation was also performed on the EPSON1680 scanner artifacts with EDR2 and EBT. Results showed that due to EDR2's superior contrast and the lower variation of pixel values over the scanner bed, scanner artifacts are less significant for dose assessment with radiological film compared to EBT. Thirteen IMRT QA cases were studied with EDR2 and EBT; EDR2 gives the same or a higher number of pixels passing the criteria (3%, 3 mm) of the γ index for eleven cases. Two results were worse with EDR2 due to both the developer artifacts and the dynamic range of EDR2.

Finally, a study was performed to investigate the impact of scanner artifacts on dose assessment with EBT films. Scanner artifacts are the result of light scattering which leads to the reading of non uniform pixel values across different columns on the scanner bed; this effect increases with dose. It was shown that the profile's measurements, processed by FILMQA, disagree with that obtained with an array of ionization chambers; however, they were improved on MATLAB by recalculating a calibration curve at each column on the scanner bed. The correction performed on MATLAB was applied to fifteen IMRT QA plans. Results were compared to that obtained with the FILMQA software. The number of pixels passing the criteria of (3%, 3 mm) was improved in nine out of fifteen cases; however, only one out of fifteen cases was drastically improved by MATLAB for the criteria (5%, 3 mm). We conclude that the Wiener filter applied on MATLAB is probably not the only correction that one must apply.

6.2 FUTURE WORK

The study performed on the CR shows strong energy dependence in the megavoltage range that was not shown on EDR2; the latter is also composed of a high atomic number material where an important attenuation of low energy photons occurs. To improve the used protocol, a Monte Carlo calculation is necessary, particularly to understand the attenuation of low energy photons on the plate.

Performing quality assurance of IMRT with EBT on MATLAB is feasible, but the proposed correction takes a long time since films were scanned at different regions on the scanner bed to correct for scanner artifacts. Characterization of the signal to noise ratio is probably the key point to improve the protocol used on MATLAB.

FILMQA is a fast and user friendly software for IMRT QA. The calibration of EBT films must be performed in a consistent way, from one batch to another. A statistical study over a large number of IMRT plans will help to determine the acceptable criteria for an IMRT plan.

LIST OF REFERENCES

[1] T. C. E. Christensen, J. Dowdey, "An Introduction to the Physics of Diagnostic Radiology", (Lea & Febiger, 1978), pp. 1, 127.

[2] J. A. S. J.T. Bushberg, E.M. Leidholdt, J.M. Boone, "The Essential Physics of Medical Imaging", (Lippincott Williams & Wilkins, 2002), pp. 4, 327, 175, 295.

[3] E. B. Podgorsak, "Radiation Physics for Medical Physicists", (Springer, 2006), pp. 361, 402, 4, 147, 235, 246, 99, 88, 8.

[4] J. V. Dvk, "The Modern Technology of Radiation Oncology : a Compendium for Medical Physicists and Radiation Oncologists", (Medical Physics Publishing, Madison, WI, 1999), pp. 5, 314, 354, 354, 140.

[5] http://scaa.usask.ca/gallery/uofs_events/articles/1948.php
[6] http://scaa.usask.ca/gallery/uofs_events/articles/1964.php
[7] http://scaa.usask.ca/gallery/uofs_events/articles/1951.php

[8] F. M. Khan, "The Physics Of Radiation therapy", (Lippincott Williams & Wilkins, 2003), pp. 481, 153, 160.

[9] A.Boyer, E.B Butler, T.A.Dipetrillo, M.J.Engler, B.Fraass, W.Grant, C.C.Ling, D.A.Low, T.R.Mackie, R.Mohan, J.A.Purdy, M.Roach, J.G.Rosenman, L.J.Verhey, J.W.Wong, R.L.Cumberlin, H.Stone, J.Palta, " Intensity Modulated radiotherapy: Current Status and Issues of Interest", Int.J.Radiation Oncology Biol.Phys **51** (2001) 880-914.

[10] S. Webb, "Historical Perspective On IMRT", (Intensity Modulated Radiation Therapy, the state of the art 'AAPM 2003 summer school proceedings', 2003), pp. 1.

[11] W. Bar, M. Schwarz, M. Alber, L. J. Bos, B. J. Mijnheer, C. Rasch, C. Schneider, F. Nusslin, and E. M. Damen, " A comparison of forward and inverse treatment planning for intensity modulated radiotherapy of head and neck cancer", Radiother Oncol **69** (2003) 251-258.

[12] E. B. Podgorsak, "Radiation Oncology Physics : A handbook for teachers and students", (IAEA, 2005), pp.407, 71.

[13] G. A. Ezzell, J. M. Galvin, D. Low, J. R. Palta, I. Rosen, M. B. Sharpe, P. Xia, Y. Xiao, L. Xing, and C. X. Yu, " Guidance document on delivery, treatment planning, and clinical implementation of IMRT: report of the IMRT

Subcommittee of the AAPM Radiation Therapy Comitee", Med Phys **30** (2003) 2089-2115.

[14] P. D. Arthur Boyer, P. D. Peter Biggs, D. S. James Galvin, M. S. Eric Klein, P. D. Thomas LoSasso, P. D. Daniel Low, M. S. Katherine Mah, and D. S. Cedric Yu, "Basic applications of multileaf collimators. report of Task Group No.50. Rdaiation Therapy Committee", Med Phys **27** (2001) 1617.

[15] M. N. Graves, A. V. Thompson, M. K. Martel, D. L. McShan, and B. A. Fraass, "Calibration and quality assurance for rounded leaf-end MLC systems", Med Phys **28** (2001) 2227-2233.

[16] J. Deng, T. Pawlicki, Y. Chen, J. Li, S. B. Jiang, and C. M. Ma, "The MLC tongue and groove effect on IMRT dose distributions", Phys Med Biol **46** (2001) 1039-1060.

[17] J. H. Kung, G.T.Y. Chen, "IMRT dose delivery error from radiation field offset inaccuracy", MEd Phys **27** (2000) 1617-1622.

[18] L. X. Y. Chen, G. Luxton, J. G. Li, A.L. Boyer, " Implementation of a Clarckson summation algorithm for dose verification in MLC-based IMRT", (Proceedings of the 22nd Annual EMBS International Conferences), July 23-28 (2000).

[19] C. C. P. Xia, "patient-Specific Quality Assurance In IMRT", (Intensity Modulated Radiation Therapy, the state of the art 'AAPM 2003 summer school proceedings', 2003), pp. 495.

[20] H. Bouchard and J. Seuntjens, "Ionization chamber-based reference dosimetry of intensity modulated radiation beams", Med Phys **31** (2004) 2454-2465.

[21] H.E. Johns, J.R. Cunningham, "The Physics of Radiology", (C. Thomas, 1983), pp. 137, 167, 173, 192.

[22] F. H. Attix, "Introduction To Radiological Physics and Dosimetry", (Wiley-Interscience, 1986), pp. 125, 146, 369, 143, 435, 21.

[23] Natioanl Institute of Standards and Technology, http://physics.nist.gov/PhysRefData/Xcom/html/xcom1.html

[24] Natioanl Institute of Standards and Technology, http://physics.nist.gov/PhysRefData/Star/Text/ESTAR.html

[25] S. Pai, I. J. Das, J. F. Dempsey, K. L. Lam, T. J. Losasso, A. J. Olch, J. R. Palta, L. E. Reinstein, D. Ritt, and E. E. Wilcox, "TG-69:radiographic film for megavoltage beam dosimetry", Med Phys **34** (2007) 2228-2258.

[26] N. F. Mott, R.W. Gurney, "The theory of the photolysis of silver bromide and photographic latent image", Proceedings of the royal society of London. Series A, Mathematical and Physical Sciences **164** (1938) 151-167.

[27] A. J. Olch, "Dosimetric performance of an enhanced dose range radiographic film for intensity modulated radiation therapy quality assurance", Med Phys **29** (2002) 2159-2168.

[28] X. R. Zhu, S. Yoo, P. A. Jursinic, D. F. Grimm, F. Lopez, J. J. Rownd, and M. T. Gillin, "Characteristics of sensitometric curves of radiographic films",Med Phys **30** (2003) 912-919.

[29] M. J. Butson, T. Cheung, and P. K. Yu, "Weak energy dependence of EBT gafchromic film dose response in the 50 kVp-10 MVp X-ray range", Appl Radiat Isot **64** (2006) 60-62.

[30] A. Niroomand-Rad, C. R. Blackwell, B. M. Coursey, K. P. Gall, J. M. Galvin, W. L. McLaughlin, A. S. Meigooni, R. Nath, J. E. Rodgers, and C. G. Soares, "Radiochromic film dosimetry: recommendations of the AAPM Radiation Therapy Committee Task Group 55", Med Phys ***25*** (1998) 2093-2115.

[31] C.G.Soares, "New developments in radiochromic film dosimetry (invited paper)", Radiation Protection Dosimetry **120** (2006) 100-106.

[32] I. Ali, J. F. Williamson, C. Costescu, and J. F. Dempsey, "Dependence of radiochromic film response kinetics on fractionated doses", Appl Radiat Isot **62** (2005) 609-617.

[33] G. L. R.B. Miller, R.C. Miller, R. Smith, D. Shimer,, M. M. C. Seidt, H. Mohr, G. Robison, P. Creely,, and T. O. J. Bautista, L.M. Young, D. DuBois, "A high power electron linear accelerator for food irradiation applications", Nuclear Instruments and Methods in Physics Research **B 211** (2003) 562-570.

[34] S. Devic, J. Seuntjens, W. Abdel-Rahman, M. Evans, M. Olivares, E. B. Podgorsak, T. Vuong, and C. G. Soares, "Accurate skin dose measurements using radiochromic film in clinical applications", Med Phys **33** (2006) 1116-1124.

[35] Y. Zhu, A. S. Kirov, V. Mishra, A. S. Meigooni, and J. F. Williamson, "Quantitative evaluation of radiochromic film response for two-dimentional dosimetry", Med Phys **24** (1997) 223-231.

[36] A. Martinez-Davalos, M. Rodriguez-Villafuerte, R. Diaz-Perches, and S. Arzamendi-Perez, "Radiochromic dye film studies for brachytherapy applications", Radiat Prot Dosimetry **101** (2002) 489-492.

[37] E. Poon, B. Reniers, S. Devic, T. Vuong, and F. Verhaegen, "Dosimetric characterization of a novel intracavitary mold applicator for ^{192}Ir high dose rate endorectal brachytherapy treatment", Med Phys **33** (2006) 4515-4526.

[38] O. A. Zeidan, S. A. Stephenson, S. L. Meeks, T. H. Wagner, T. R. Willoughby, P. A. Kupelian, and K. M. Langen, "Characterization and use of EBT radiochromic film for IMRT dose verification", Med Phys **33** (2006) 4064-4072.

[39] S. Devic, J. Seuntjens, E. Sham, E. B. Podgorsak, C. R. Schmidtlein, A. S. Kirov, and C. G. Soares, "Precise radiochromic film dosimetry using a flat-bed document scanner", Med Phys **32** (2005) 2245-2253.

[40] S. Devic, N. Tomic, Z. Pang, J. Seuntjens, E. B. Podgorsak, and C. G. Soares,"Absorption spectroscopy of EBT model GAFCHROMIC film", Med Phys **34** (2007) 112-118.

[41] A. Gonzalez-Lopez, "Useful optical density range in film dosimetry: limitations due to noise and saturation", Phys Med Biol **52** (2007) N321-327.

[42] J. F. Dempsey, D. A. Low, A. S. Kirov, and J. F. Williamson, "Quantitative optical densitometry with scanning-laser film digitizers", Med Phys **26** (1999) 1721-1731.

[43] S. Devic, Y. Z. Wang, N. Tomic, and E. B. Podgorsak, "Sensitivity of linear CCD array based film scanners used for film dosimetry", Med Phys **33** (2006) 3993-3996.

[44] S. Shinoya, W. M. Yen, H.Yamamoto, "Phosphor Handbook", (CRC Press, Taylor &Francis group, 2007), pp. 3, 11, 661, 659.

[45] R.Schaetzing, in RSNA (Radiological Society of North America), 2003, p. 7-22.

[46] J.A.Rowlands, "The physics of computed radiography", Physics in Medecine and Biology **47** (2002) 123-166.

[47] N. T. M.Hareyama, M.Takebe, T.Chida, "Two dimensional measurement of natural radioactivity of granitic rocks by photostimulated luminescence technique", Geochemical journal **34** (1999) 1-9.

[48] www.varian.com/us/oncology/radiation_oncology

[49] P. R. Almond, P. J. Biggs, B. M. Coursey, W. F. Hanson, M. S. Huq, R. Nath, and D. W. Rogers, "AAPM's TG-51 protocol for clinical reference dosimetry of high energy photon and electron beams", Med Phys **26** (1999) 1847-1870.

[50] A. J. Olch, "Evaluation of a computed radiography system for megavoltage photon beam dosimetry", Med Phys **32** (2005) 2987-2999.

[51] J. Van Dyk, R.B. Barnet, J.E. Cygler, P.C. Shragge, "Commissioning and quality assurance of treatment planning computers", Int.J.Radiation Oncology Biol.Phys **26** (1993) 261-273.

[52] W. B. Harms, D. A. Low, J. W. Wong, and J. A. Purdy, "A software tool for the quantitative evaluation of 3D dose calculation algorithms", Med Phys **25** (1998) 1830-1836.

[53] D. A. Low, W. B. Harms, S. Mutic, and J. A. Purdy, "A tachnique for the quantitative evaluation of dose distributions", Med Phys **25** (1998) 656-661.

[54] J.R. Palta, S. Kim, J.G. Li, C. Liu, "Tolerance limits and action levels for planning and delivery of IMRT", Intensity Modulated Radiation Therapy, the state of the art 'AAPM 2003 summer school proceedings' (2003) 593-612.

[55] I.-A. Jurkovic, "Evaluation of a desktop computed radiography system for IMRT dosimetry", Master thesis, 2004, Department of Physics and Astronomy of Louisiana University

[56] C. C. J.Eriksson, K.Eilertsen, P.Engstrom, P.Munck af Rosenschold, C.Lervag, "2D dosimetry using a computed radiography imaging system", 9th Biennial Estro meeting on radiation technology for clinical radiotherapy. 8-13 september 2007 Barcelona.

[57] C. C. F.Nordstrom, H.Gustavsson, P.Engstrom, P.Bjork, S.Johnson, O.Holmberg, S.Back, "Intensity modulated radiotherapy dose verification methods: an intercomparison study", 9th Biennial Estro meeting on radiation technology for clinical radiotherapy. 8-13 september 2007 Barcelona.

[58] C. Fiandra, U. Ricardi, R. Ragona, S. Anglesio, F. R. Giglioli, E. Calamia, and F. Lucio, "Clinical use of EBT model Gafchromic film in radiotherapy", Med Phys **33** (2006) 4314-4319.